REVIEW

Light trapping in mesoporous solar cells with plasmonic nanostructures

William R. Erwin, Holly F. Zarick, Eric M. Talbert and Rizia Bardhan*

Plasmon resonances in metal nanostructures have been extensively harnessed for light trapping in mesoporous solar cells (MSCs), including dye-sensitized solar cells (DSSCs) and recently in perovskite solar cells (PSCs). By altering the geometry, dimension, and composition of metal nanostructures, their optical characteristics can be tuned to either overlap with the sensitizer absorption and enhance light harvesting, or absorb light at a wavelength complementary to the sensitizer enabling broadband solar light capture in MSCs. In this comprehensive review, we discuss the mechanisms of plasmonic enhancement in MSCs including far-field coupling of scattered light, near-field coupling of localized electromagnetic fields, hot electron transfer, and plasmon resonant energy transfer. We then summarize the progress in plasmon enhanced DSSCs in the past decade and decouple the impact of metal nanostructure shape, size, composition, and surface coatings on the overall efficiency. Further, we also discuss the recent advances in plasmon-enhanced perovskite solar cells. Distinct from other published reviews, we discuss the significance of femtosecond spectroscopies to probe the fundamental underpinnings of plasmon enhanced phenomena and understand the mechanisms that give rise to energy transfer between metal nanoparticles and solar materials. The review concludes with a discussion on the challenges in plasmonic device fabrication, and the promise of low-loss semiconductor nanocrystals for plasmonic enhancement in MSCs that facilitate light capture in the infrared.

Broader context

Emerging photovoltaics, including PSCs and their predecessors, DSSCs, collectively described as mesoporous solar cells (MSCs), have rapidly evolved as a serious contender to traditional crystalline silicon photovoltaics due to the inexpensive materials and low processing costs. However low efficiencies, specifically in thin-film architectures, have remained a major hurdle to commercialization in these classes of MSCs. The past decade has witnessed significant improvements in device performance of MSCs by integrating subwavelength plasmonic nanostructures in the active layer. Metal nanostructures function as a secondary light source to augment the total light trapped within the mesoporous layer, enabling enhanced carrier generation. This consequently decreases the amount of active material required to achieve high efficiency solar conversion. Plasmon-enhanced thin-film MSCs will ultimately enable integration on flexible substrates, resulting in low-cost and high efficiency flexible solar cells compatible with scalable manufacturing routes such as inkjet printing and roll-to-roll processing. By understanding the fundamental mechanisms of plasmonic enhancement in MSCs, this technology will ultimately enable rapid advancements in the active light management of a range of optoelectronic devices including photovoltaics, sensors, photoelectrochemical cells, and photodetectors.

1. Introduction

Mesoporous solar cells (MSCs), including dye-sensitized solar cells (DSSCs) and perovskite solar cells (PSCs), form an important class of third generation solar cells or "emerging photovoltaics (PVs)".[1] MSCs are typically composed of a nanocrystalline anatase TiO_2 active layer decorated with a monolayer of a sensitizer and coupled with a compact TiO_2 electron transport layer. For shuttling holes, either a liquid electrolyte such as

Department of Chemical and Biomolecular Engineering, Vanderbilt University, Nashville, TN, USA 37212. E-mail: rizia.bardhan@vanderbilt.edu

I^-/I_3^- redox couple, or a solid-state hole-transport material (HTM) such as Spiro-OMeTAD (2,2′,7,7′-tetrakis-(N,N-di-4-methoxy-phenylamino)-9,9′-spirobifluorene) is used.[2–4] In the case of DSSCs, ruthenium-based dyes and porphyrins are typically employed as sensitizers,[5–9] whereas for PSCs methyl ammonium lead halide (MAPbX$_3$, X = I, Br, Cl) perovskites are the most commonly used light absorbers.[3,4,10–15] MSCs have attracted significant attention in the past decade with the promise to lower the cost of solar power by combining the advantages of inexpensive material constituents with solution-processable, scalable, and reproducible device fabrication. This has resulted in tremendous research efforts to improve their efficiency and stability,

and MSCs are already being commercialized (G24, Sony, Aisin Seiki) for niche markets to power consumer electronics and low-power technologies.[16,17] However, to adopt these emerging PVs globally for high-power applications and utility-scale power generation, efficiencies greater than 20% are necessary.

Subwavelength metal nanostructures have been demonstrated as a highly effective route to augment light harvesting in solar devices, giving rise to improved optical absorption, carrier generation, and overall power conversion efficiency.[18–20] The past decade has witnessed a significant rise in plasmonic enhancement of MSCs with Au, Ag, and Au/Ag bimetallic nanostructures resulting in 20–60% improvement in efficiency.[21–30] Fig. 1a shows a schematic of metal nanostructures integrated in MSCs. Following photoexcitation in metal nanostructures incident photons are coupled to conduction band electrons, giving rise to collective oscillations of the electrons defined as localized surface plasmon resonances (LSPRs).[31–34] By engineering the geometry, dimension, and composition, the LSPR of metal nanostructures can be manipulated to capture specific wavelengths of solar light to supplement or complement the absorption by the sensitizer. This ultimately increases the total light trapped within the mesoporous layer of MSCs (Fig. 1b–f).[35–39] In this review, we highlight the fundamental mechanisms that contribute to plasmonic enhancement in MSCs, followed by a summary of the progress in metal-enhanced DSSCs and PSCs in the past decade. Further, we discuss the challenges in the fabrication of metal nanostructure integrated devices and summarize the importance of femtosecond time-resolved spectroscopies to understand the foundational principles of plasmon-enhanced phenomena. The review concludes with a discussion of the potential of new

William R. Erwin

William Erwin is pursuing his PhD in Chemical and Biomolecular Engineering at Vanderbilt University under the supervision of Prof. Rizia Bardhan. He received a BS in Chemical Engineering from the University of Arkansas in 2012, and was awarded the NSF Graduate Research Fellowship in 2013. His research focuses on the interactions of plasmons with third generation solar materials including dye-sensitized solar cells, organic semiconductors and perovskites.

Holly F. Zarick

Holly Zarick is a PhD student in the Chemical and Biomolecular Engineering department at Vanderbilt University. She received her Bachelor's degree in Chemical Engineering from the University of New Mexico in 2012. Currently, she is conducting her PhD studies under the supervision of Dr Rizia Bardhan, with a focus on enhancing the performance of dye-sensitized and organometal trihalide perovskite solar cells with the incorporation of shape and composition controlled plasmonic nanostructures, and further studying the impact on electron dynamics in these systems using ultrafast spectroscopies.
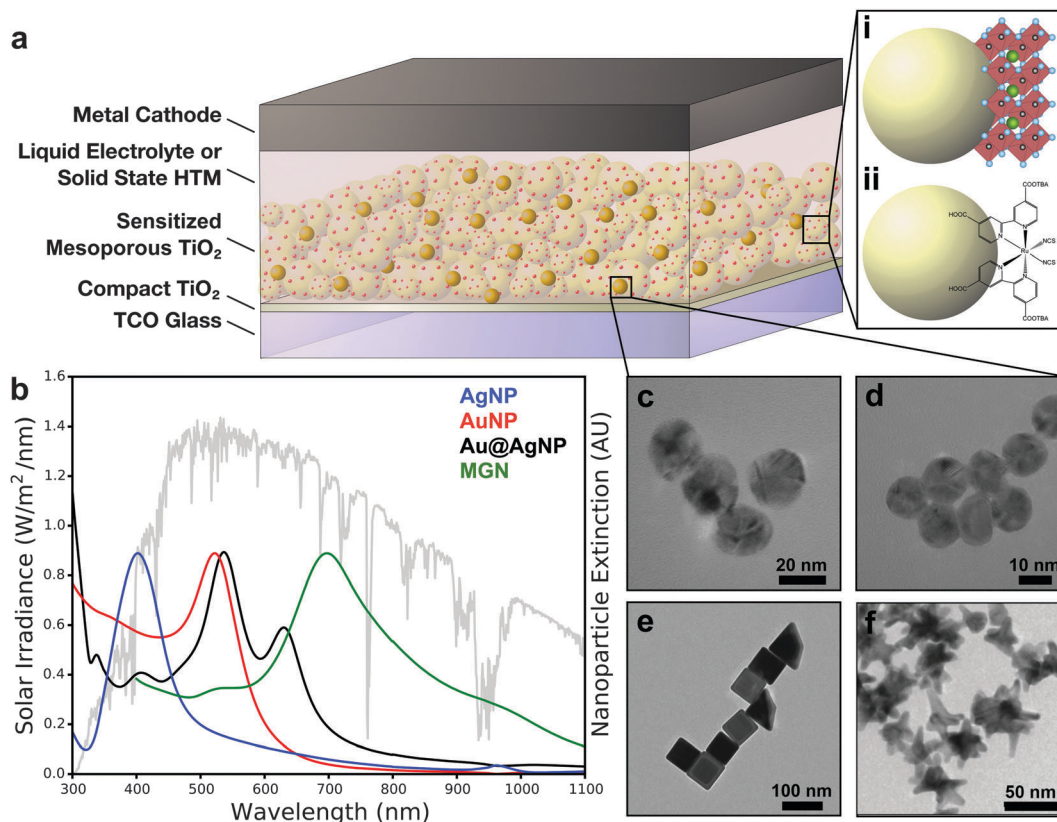
Eric M. Talbert

Eric Talbert is a graduate student of chemical engineering at Vanderbilt University. He received a BS in Chemical and Biomolecular Engineering from Rice University in 2014, then joined Prof. Rizia Bardhan's group to investigate light interactions with nanoscale materials. Recently, he has focused on studying absorption dynamics and charge transport in perovskite solar cells using ultrafast spectroscopies.

Rizia Bardhan

Prof. Rizia Bardhan joined the Chemical and Biomolecular Engineering department at Vanderbilt University in August 2012. Prior to her faculty appointment she received a PhD in Chemistry from Rice University under the supervision of Prof. Naomi Halas. She did her postdoctoral work at the Molecular Foundry in Lawrence Berkeley National Lab in designing nanomaterials for energy storage and conversion. She is a recipient of the Ralph E. Powe junior faculty enhancement award, NSF BRIGE award, and Forbes "Top 30 Under 30: Rising Stars of Science and Innovation" Award. She has over a decade of experience in plasmonics, nanophotonics, and a strong background in mesoporous solar cells and has published >45 highly cited papers in this field.

1578 | *Energy Environ. Sci.,* 2016, **9**, 1577–1601

This journal is © The Royal Society of Chemistry 2016

Fig. 1 (a) Generalized mesoporous solar cell schematic for (i) perovskite solar cells and (ii) dye-sensitized solar cells. (b) Solar irradiance overlaid with extinction spectra of nanostructures corresponding to TEM images of (c) Ag nanoparticles (Ag NP), (d) Au nanoparticles (Au NP), (e) Au@Ag nanoparticles (Au@Ag NP), and (f) multibranched gold nanoantennas (MGN). Panels e and f adapted with permission from ref. 41 and 42, respectively. Copyright 2014 American Chemical Society.

plasmonic materials beyond Au and Ag nanostructures and a brief outlook on future directions in plasmonic enhancement in PSCs, both in the mesoscopic and planar architectures.

2. Mechanisms of plasmonic enhancement

LSPRs in metal nanostructures give rise to a collection of optical and electronic effects, processes that occur during the excitation and subsequent decoherence of a plasmon and ultimately contribute to enhanced photonic effects in MSCs.[31–33] Plasmonic enhancement in solar devices is attributed to (i) radiative effects, in which the LSPR relaxes and re-radiates light into the absorptive layer or the metal nanostructures act as a secondary light source that enhances local electric fields, and (ii) non-radiative effects where the LSPR relaxes and energy is subsequently transferred to vicinal semiconductor, enhancing the current generation.[18–20,40] Metal nanostructures essentially act as a direct sensitizer during non-radiative processes. This section will explain the four mechanisms of plasmonic enhancement, shown in Fig. 2, including light scattering and electromagnetic fields categorized within radiative effects, and hot electron transfer and plasmon resonant energy transfer which fall under non-radiative effects.

2.1 Radiative effects

LSPRs of metal nanostructures have finite lifetimes following which they decay either radiatively by emitting a photon, or non-radiatively by generating electron–hole pairs.[31–33] The radiative decay process either gives rise to electromagnetic fields in the nanostructures' "near-field" or light scattering into the nanostructures' "far-field." Radiative effects are best understood as a dipole–dipole coupling between the metal nanoparticle dipolar fields with the molecule or sensitizer dipole. The metal-molecule radiative coupling is proportional to r^{-3}, where r is the distance from the molecule to the nanostructure. At the plasmon resonance however, radiative fields follow r^{-6} dependence and may far exceed unity.[43–47] In this section, we discuss the basic concepts and mechanisms of plasmonic enhancement in MSCs by radiative processes.

2.1.1 Far-field scattering. Light incident on metal nanostructures with a sufficiently high albedo is scattered into the far-field; depending on geometric and material properties of the particle, the scattering cross section may be up to an order of magnitude larger than the physical cross-section of the nanostructure.[31] This far-field scattered light can ultimately be reabsorbed by the sensitizer in MSCs, enabling enhanced light absorption by sensitizing molecules even at distances of several hundred nanometers. Photons scattered from each

This journal is © The Royal Society of Chemistry 2016
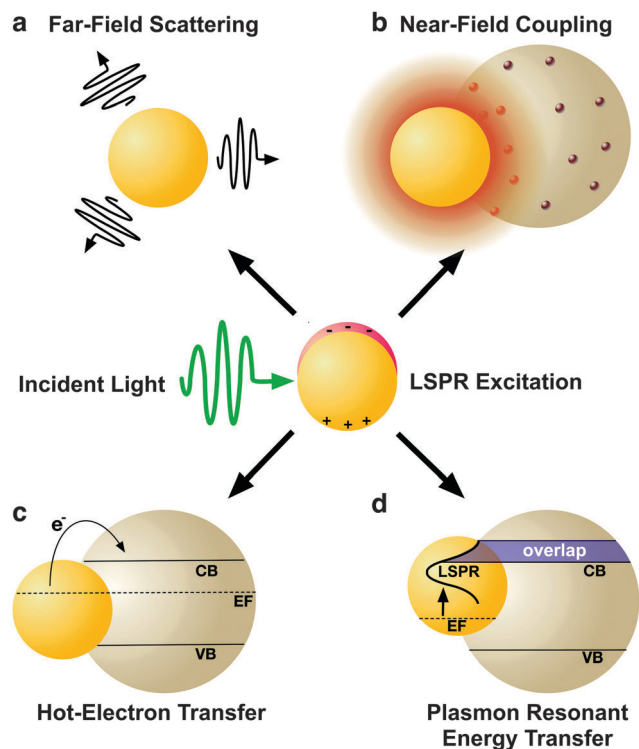
Energy Environ. Sci., 2016, 9, 1577–1601 | 1579

Fig. 2 Schematic illustration of plasmon enhancement mechanisms of radiative effects (a) far-field scattering and (b) near-field coupling; and nonradiative effects: (c) hot-electron transfer, and (d) plasmon resonant energy transfer.
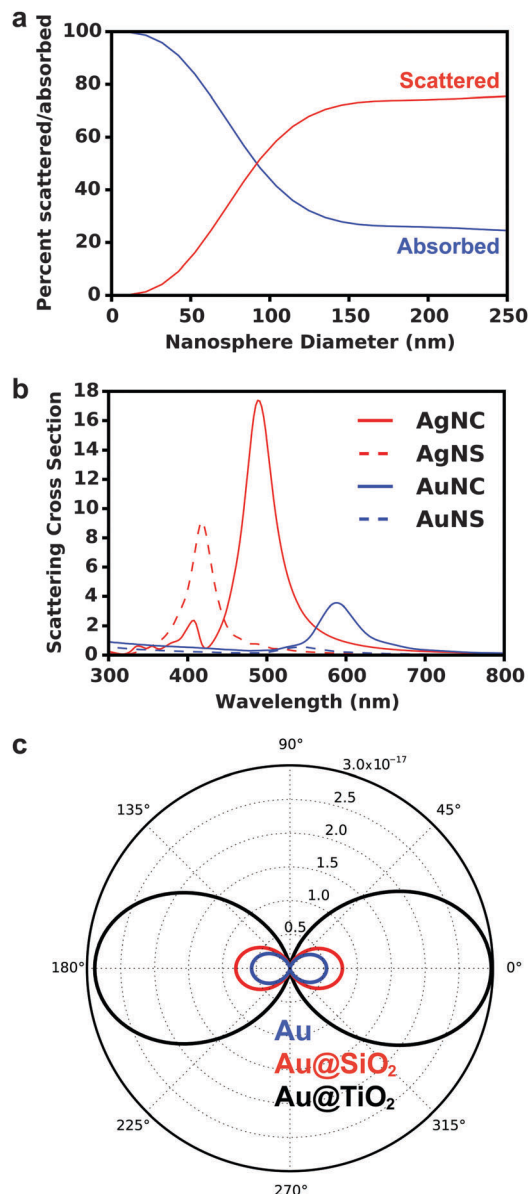

Fig. 3 (a) Percent of light scattered and absorbed calculated as a function of Au nanosphere diameter integrated from 300–800 nm. (b) Calculated scattering cross sections of 50 nm Au and Ag nanospheres (NS) and nanocubes (NC) indicate that both shape and composition control nanoparticle albedo. (c) Calculated angular scattering of 50 nm Au nanosphere bare, with a 10 nm SiO$_2$ coating, and with a 10 nm TiO$_2$ coating. All calculations were performed in Lumerical FDTD Solutions.

nanostructure can also encounter multiple scattering from proximal nanostructures in the far-field, which ultimately increases the total light trapped within the MSCs.[48–50] Further, by tuning the LSPR to wavelengths complementary to the sensitizer's absorption, nanostructures can be designed to capture solar photons not absorbed by the sensitizer.[51,52] Light scattering properties of metal nanostructures are a function of their size and are best understood by Mie theory.[53–56] Mie theory is the simplest analytical solution of Maxwell's equations and describes the extinction behavior of spherical metal nanoparticles when excited with an incident electric field. For a metal nanosphere with radius a in a dielectric medium, where the permittivity for the metal and medium are given by ε_{metal} and ε_{medium}, respectively, the scattering cross section (σ_{scat}) is given by:

$$\sigma_{scat} = \frac{8\pi}{3} k^4 a^6 \left| \frac{\varepsilon_{metal} - \varepsilon_{medium}}{\varepsilon_{metal} - 2\varepsilon_{medium}} \right|^2 \qquad (1)$$

where $k = 2\pi/\lambda$. Since σ_{scat} scales with a^6, metal nanoparticles with sizes $a > 30$ nm are ideal for coupling far-field scattered light into the sensitized active layer of MSCs, resulting in enhanced light harvesting.[57] We have calculated absorption and scattering cross-sections of spherical Au nanoparticles to demonstrate this size effect. Fig. 3a shows that the percent light scattered from nanoparticles monotonically increases with size while the amount of light absorption decreases.

At the crossover size of ∼90 nm for spherical Au nanoparticles, the amount of light absorbed and scattered is equivalent,

indicating nanoparticle size can be tuned to achieve desired absorptive and scattering properties for maximum solar harvesting.

Beyond the size of metal nanostructures, shape also controls the far-field scattered light attributed to the enhanced polarizability, or ability to polarize incoming light, of the nanostructures (Fig. 3b).[35,58–60] The effect of polarizability is particularly dominant for non-spherical nanostructures with sharp edges and corner such as cubes, pyramids, and octahedrons, as well as layered concentric nanostructures where the polarizability is enhanced at the metal/dielectric interface of each layer.[61] Further, light scattering characteristics are affected by the composition
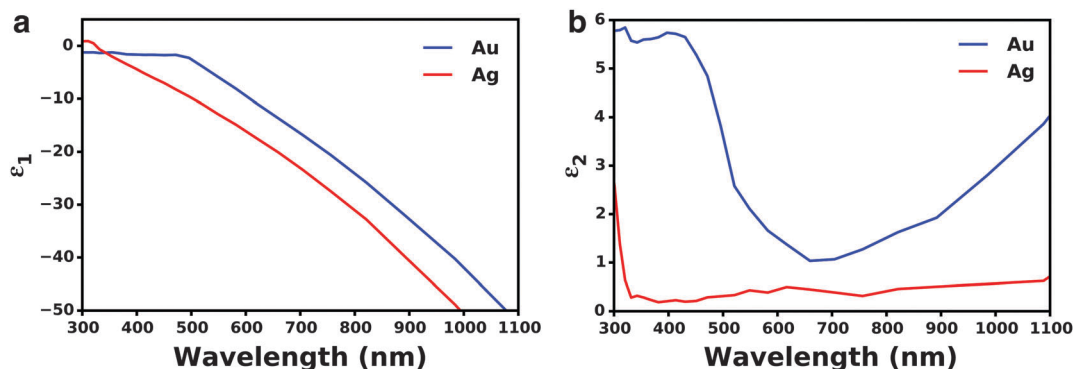
Fig. 4   (a) Real part of the dielectric function for Au and Ag. (b) Imaginary part of the dielectric function of Au and Ag. Data adapted from ref. 63.

of nanostructures, where Ag has stronger radiative properties due to less Ohmic losses than Au (Fig. 3b). This is best described by the complex dielectric functions of bulk Ag and Au, which consists of a real (Fig. 4a) and imaginary (Fig. 4b) part. The real part of the dielectric function (ε_1) determines the polarization response and scales with carrier concentration in the metal. The imaginary part of the dielectric function (ε_2) determines the optical losses including interband and intraband losses. For Au, intraband or Drude losses, are high in the near-infrared and lower in the visible. Alternatively, interband losses in Au are high at shorter wavelengths. The smaller imaginary dielectric function of Ag across all wavelengths implies lower optical losses (*i.e.* plasmon damping), which results in higher scattering efficiency and narrower plasmon linewidths.[62–65] This fundamental difference in the optical behavior of Au and Ag has been extensively harnessed in plasmonic sensing, and more recently applied to MSCs where Ag has shown stronger enhancement in carrier generation.[21,38,66–72] Section 3 of this review will discuss the impact of nanostructure size, shape, and composition on DSSCs and PSCs in more detail.

Finally, far-field effects in MSCs may be tuned as a function of the permittivity of the medium (ε_{medium}) surrounding the metal nanostructures.[73–76] A higher ε_{medium} (i) red-shifts the LSPR frequency enabling capture of solar photons where the sensitizer poorly absorbs, and (ii) enables preferential scattering in targeted directions.[77] Calculated angular scattering (Fig. 3c) of 50 nm Au nanoparticles uncoated, and coated with 10 nm SiO_2 and TiO_2 demonstrates $>3\times$ light scattering for TiO_2 coated nanoparticles. The dielectric constant of TiO_2 is ~ 6.8 whereas that of SiO_2 is ~ 2.1. The red-shift in LSPR frequency, λ_p, with increase in ε_{medium} is best understood by the Drude approximation for quasi-static metal nanoparticles, given by:

$$\lambda_p = \lambda_{p,b}\sqrt{2\varepsilon_{medium} + 1} \qquad (2)$$

where $\lambda_{p,b}$ is the bulk plasmon wavelength. Further, the sensitivity of the scattering cross section, σ_{scat}, to ε_{medium} can be understood from Mie theory, given by:

$$\sigma_{scat} = \frac{32\pi^4 \varepsilon_{medium}^2 V^2}{\lambda^4} \frac{(\varepsilon_1 - \varepsilon_{medium})^2 + (\varepsilon_2)^2}{(\varepsilon_1 + \varepsilon_{medium})^2 + (\varepsilon_2)^2} \qquad (3)$$

where V is the nanoparticle volume, and shows σ_{scat} scales with ε_{medium}^2. Since TiO_2 has a high dielectric permittivity, embedding metal nanostructures within the mesoporous TiO_2 layer in MSCs controls light scattering direction within the active layer, as well as enables tuning of the metal LSPR beyond the visible spectrum where many sensitizing molecules and perovskites are unable to absorb.

2.1.2   Electromagnetic near-field enhancement. The interaction of plasmonic nanostructures with incident light results in local enhancement of electromagnetic fields, defined as "near-fields," in the immediate vicinity of the nanostructure. Metal nanostructures integrated in MSCs function as nanosized light concentrators focusing incident light on the metal surface within a small mode volume; the intensities of these fields are typically orders of magnitude higher than the incident light. Therefore, one can envision nanostructures as a secondary light source increasing the photon flux and the overall light absorbed by the solar cell.[18,19,34,40,79] Sensitizing molecules in the proximity of the nanostructures directly couple with the strong near-fields and the resulting plasmon-molecule coupling increasing the electron–hole pair generation in the sensitizer. A higher density of carriers is then available to transfer from the lowest unoccupied molecular orbital (LUMO) of the sensitizer to the conduction band of TiO_2, which subsequently improves overall current density of MSCs. This process is described schematically in Fig. 5.

Electromagnetic near-fields at the plasmon resonance decay proportional to r^{-6}, where r is the distance from the nanostructure, and typically extend <50 nm from the nanostructure surface (Fig. 6a). Analogous to far-field scattering, the near-fields generated by the LSPR are governed by the metal nanostructure morphology and composition.[57,59,60] Non-spherical nanostructures with sharp features, such as nanocubes, generate a high concentration of charges localized at the edges and corners, attributed to the lightning-rod effect.[80–83] Finite difference time domain (FDTD) simulations demonstrate the impact of nanostructure morphology and composition on the local electromagnetic field intensities at the plasmon resonance (Fig. 6b–e). These intense fields in nanocubes decay slower and extend much farther than their spherical counterparts (Fig. 6b–e). The lightning-rod effect was first reported by Gersten and Nitzan,[84] and then by

This journal is © The Royal Society of Chemistry 2016

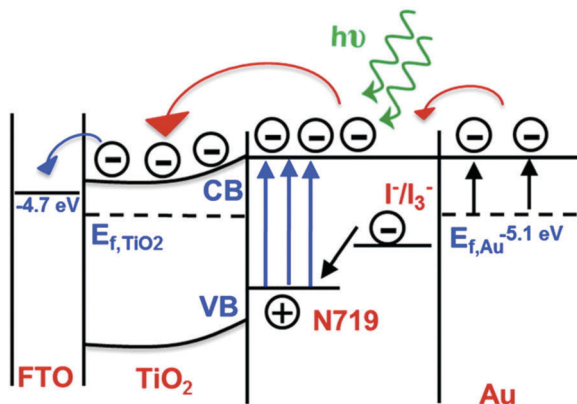*Energy Environ. Sci.,* 2016, **9**, 1577–1601 | **1581**

Fig. 5 Energy diagram of a plasmon-enhanced DSSC system detailing how coupling between the plasmonic nanostructure and N719 dye results in enhanced absorption, thereby increasing the electron transfer from the sensitizer to the mesoporous TiO$_2$. Figure adapted with permission from ref. 78. Copyright 2014 American Chemical Society.

Liao and Wokaun[85] to describe the fields localized at the tips of prolate ellipsoids. Liao *et al.* defined the lightning-rod factor, γ, given by:

$$\gamma = \frac{3}{2}\left(\frac{a}{b}\right)^2 (1 - A_a) \qquad (4)$$

where A_a is the depolarization factor of the ellipsoid, a and b are the dimensions of the long axis and short axis, respectively. For a nanosphere $\gamma = 1$, for a prolate ellipsoid with aspect ratio 3:1 $\gamma = 12$, and for an ellipsoid with aspect ratio 4:1 $\gamma = 22$. The lightning rod effect can be extended to other anisotropic shapes and ultimately explains the higher efficiencies observed when MSCs are integrated with non-spherical nanostructures. Near-field effects are also stronger for Ag relative to Au (Fig. 6a) due to the wavelength-dependent behavior of the real and imaginary dielectric functions of the metals as described in Section 2.1.1 and shown in Fig. 4. We note that a limitation of radiative enhancements is that photon energy is unchanged

when scattered, so only light that is within the band gap of the semiconductor is utilized.

2.2 Non-radiative effects

While radiative effects are the dominant mechanism for plasmonic enhancement in MSCs, non-radiative effects also play a significant role and facilitate coupling of below band gap energy into the semiconductor. Therefore by effectively harnessing non-radiative enhancement processes, ultra-high efficiencies may be realized in single junction solar cells. Two distinct non-radiative effects contribute to enhanced carrier generation in MSCs: hot-electron transfer (HET), and plasmon resonant energy transfer (PRET). Both of these non-radiative energy transfer processes have been studied in photodetectors[86] and solar photocatalysis,[87,88] but remain poorly understood in MSCs. In this section, we discuss the fundamentals of non-radiative enhancement in MSCs with plasmonic nanostructures.

2.2.1 Hot electron transfer. When a plasmon decays non-radiatively *via* Landau damping upon decoherence of the LSPR, this energetic relaxation generates hot electron–hole pairs.[89] Landau damping, a process that has been extensively studied with femtosecond spectroscopy, is a quantum mechanical phenomenon which occurs on a timescale of 1–100 fs.[90,91] Hot electrons are not in thermal equilibrium with the atoms in the metal and are characterized by an effective elevated temperature.[88,92] The generation of hot electrons in noble metal nanostructures, such as Au and Ag, is driven by either intraband excitations within the conduction band or by interband excitations resulting from transitions between d-bands and the conduction band.[32] In the case of Au, the d-band energy level lies 2.4 eV below the Fermi energy; therefore interband transitions can contribute significantly to the hot carrier generation process. However, in Ag the d-band lies 4 eV below the Fermi energy; hot electrons are therefore mostly generated by intraband excitations.[93] These hot electrons ultimately cool down through electron–electron scattering followed by electron–phonon collisions, releasing their energy to the lattice by dissipation of heat,
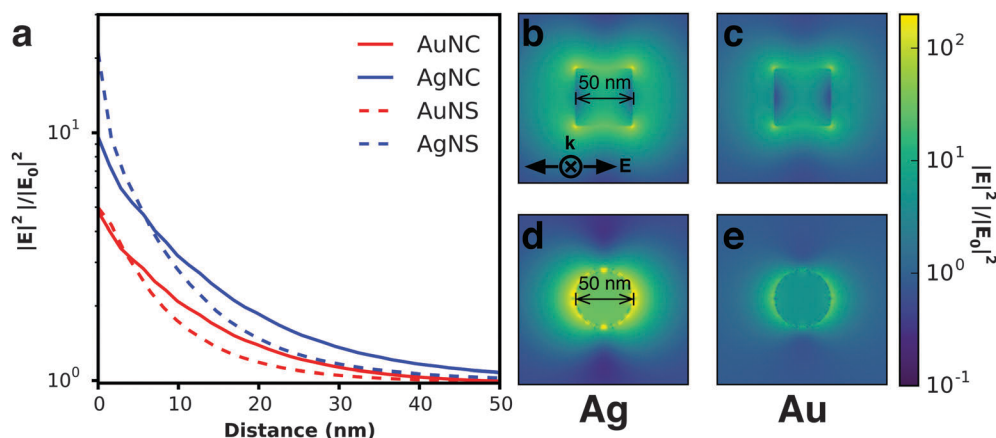

Fig. 6 (a) Calculated near field enhancement as a function of distance from the particle surface averaged over the 300–800 nm spectral range; values are averaged over the x, y, and z planes intersecting the particle. Near field profiles at peak plasmon resonance for (b) Ag nanocube at 490 nm, (c) Au nanocube at 580 nm, (d) Ag nanosphere at 420 nm, and (e) Au nanosphere at 530 nm are shown. All calculations performed in Lumerical FDTD Solutions.
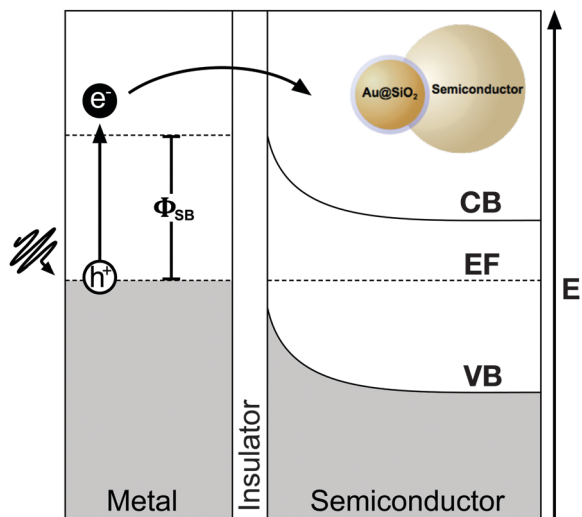
Fig. 7 Schematic energy diagram of the hot electron transfer process: first, the excitation and subsequent decoherence of a plasmon produces hot electrons and holes, followed by diffusion of hot electrons to the metal–semiconductor interface. Next, hot electrons with sufficient energy traverse the Schottky barrier and tunnel through a thin insulator (≤2 nm) to enter the conduction band of the neighboring semiconductor.

a phenomenon that has been extensively harnessed in photo-thermal cancer therapies.[94–99]

As shown in Fig. 7, prior to relaxation, hot electrons can be efficiently captured by forming a Schottky barrier, Φ_{SB}, with a semiconductor such as TiO_2, which has a high density of states in its conduction band and permits rapid electron injection over Φ_{SB}. Hot electrons with sufficient energy to overcome the Φ_{SB} can be injected into the semiconductor conduction band.[86,100–105] Since the energy needed for HET is smaller than the bandgap, E_g, of the semiconductor, spectral overlap between the metal nano-structure and semiconductor is not required in order for energy transfer to occur. However, HET can only occur when the Fermi levels of the metal and semiconductor are equilibrated, and there is a clear path for electrons to travel between the two.[86,93] In most plasmon enhanced DSSC systems, metal nanoparticles are coated in an insulating interlayer such as SiO_2. For HET to occur, the layer must be thinner than the electron tunneling barrier of the material, which is 3 nm for SiO_2.[106] Despite the promise of HET in enhancing carrier generation in plasmon enhanced MSCs, recombination of the carriers at interfaces and defect sites remains a challenge. Further, relaxation of hot holes before reaching the hole-transport material, which shuttles the holes to the counter electrode in solar cells, remains a major barrier to successful implementation of HET in MSCs.

The efficient generation and capture of hot electrons is determined by the shape, size, and composition of metal nanostructures, as well as device design. Nordlander and co-workers recently calculated hot electron generation in Ag nanoparticles of 15 nm and 25 nm diameter.[93] They demonstrated that when hot carriers are generated with energies close to the Fermi level, an increase in hot carrier production occurs with increasing size. However, larger nanoparticles produce less energetic carriers than smaller

Ag nanoparticles. Their analysis also revealed the spatial distribution of hot electrons is primarily localized along the direction parallel to the polarization of the incident field. Govorov and co-workers confirmed that hot electrons are most efficiently generated in Au or Ag nanostructures <20 nm size. Since the mean free path of an electron is on the order of 20 nm, hot electrons generated in nanoparticles with dimension >20 nm have energies closer to the Fermi level of the metal, and originate from defects in the nanoparticle.[107] The composition of metal nanostructures also determines the rate of Landau damping; for example, metals with strong intra-band transitions such as Pd, Pt, and transition metals have weak radiative properties and efficiently convert incident photons to hot electrons.[15] Hot electrons can also be preferentially generated in metal nanostructures with a strong subradiant (dark) mode, such as complex layered architectures or highly anisotropic nanostructures. The superradiant or bright modes in such metal nanostructures directly couple to the incident light and are spectrally broadened due to radiative damping, whereas subradiant modes do not couple to light, hence they are spectrally narrow and relax non-radiatively to produce hot electrons. For example, multilayered metal/dielectric nanoshells,[61,108] nano-structures with broken symmetry,[109–111] and ordered clusters of nanostructures[112–114] all have strong subradiant modes and can produce hot electrons.

By engineering the morphology and dimensions of metal nanostructures and coupling with appropriate semiconductors whose Φ_{SB} is relatively close to the Fermi level of the metal, HET can be promoted in MSCs. Challenges remain for large scale implementation of hot electron generating devices, including wet chemical synthesis of geometries which promote HET, and the synthesis of an appropriately thin insulating layer to allow for HET to neighboring semiconductor while minimizing unwanted recombination.

2.2.2 Plasmon resonant energy transfer. In addition to HET, plasmon resonant energy transfer (PRET) also plays a key role in non-radiative plasmonic enhancements in MSCs. PRET is analogous to Förster resonant energy transfer (FRET) where the LSPR dipole replaces the fluorescent molecule (Fig. 8a). The LSPR dipole originates from the oscillations of conduction electrons and dephases on plasmon decoherence via absorption or scattering. Following light absorption by the metal nanostructures, PRET occurs when the resonant energy is transferred from the metal to the adjacent semiconductor via dipole–dipole coupling, generating electron–hole pairs below and near the semiconductor band edge.[87,115,116] In contrast to HET, where minimal separation (≤2 nm) between the metal and semiconductor is essential, PRET is unaffected by any insulating interlayer, such as SiO_2. PRET occurs as long as the semiconductor is within the "nanostructures" near-field and a spectral overlap exists between the LSPR and the semiconductor absorption. Further, unlike HET where a band alignment of the metal Fermi level with the semiconductor is required, PRET is not limited by Fermi level equilibration.[117] Plasmon enhancement in MSCs by PRET is determined by the morphology and composition of metal nanostructures, and distance separating the semiconductor
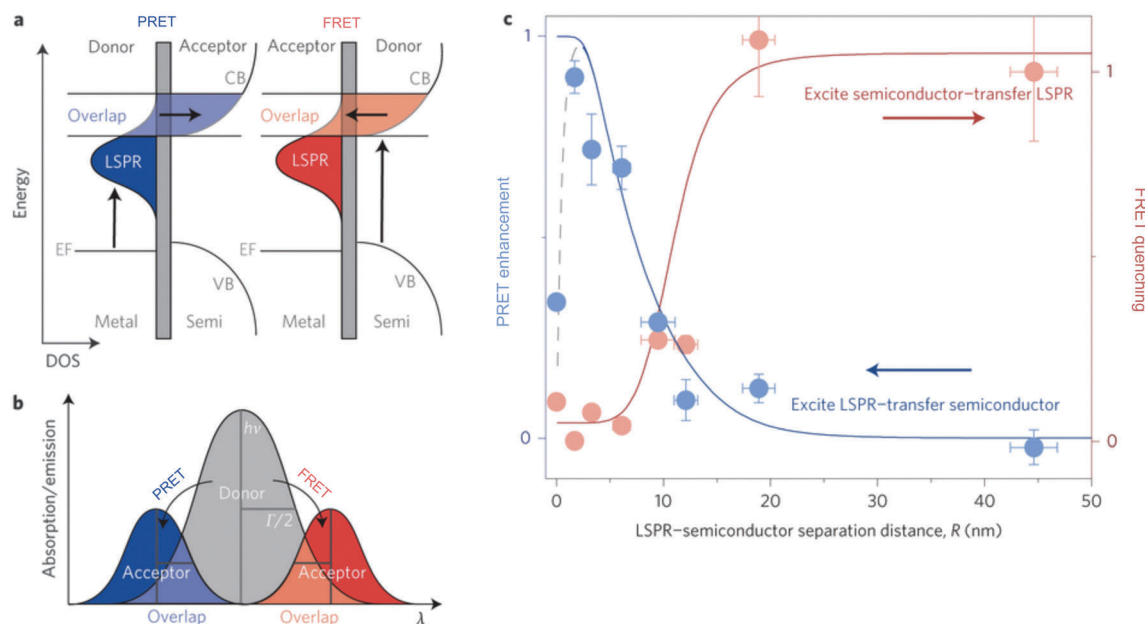
Fig. 8 (a) In PRET, energy in the plasmon is transferred to the acceptor molecule, and in the competing process, FRET, energy is transferred from the semiconductor to the plasmon. (b) Diagram distinguishing PRET and FRET spectrally, where PRET results in energy upconversion and FRET results in energy downconversion. (c) The bulk of energy transfer in both the PRET and FRET mechanisms occur within 20 nm of the LSPR. Adapted by permission from Macmillan Publishers Ltd: ref. 87, copyright 2015.

and metal.[118,119] Wu and co-workers recently performed transient absorption spectroscopy (TAS) and compared the transient signal between four core@shell metal nanospheres, Au@TiO$_2$, Au@SiO$_2$@TiO$_2$, Ag@TiO$_2$, and Ag@SiO$_2$@TiO$_2$, to differentiate the HET and PRET processes.[115] Their results demonstrated that HET was dominant in Au@TiO$_2$ nanoparticles following light absorption due to direct contact between metal and semiconductor, whereas in Ag@SiO$_2$@TiO$_2$ the insulating silica interlayer prevents HET but promotes PRET due to strong spectral overlap between Ag and TiO$_2$. In addition, both HET and PRET are possible in Ag@TiO$_2$, whereas Au@SiO$_2$@TiO$_2$ nanoparticles allowed neither HET nor PRET due to poor spectral overlap between Au and TiO$_2$ and presence of >3 nm silica layer preventing plasmon-enhanced photoconversion in TiO$_2$. An enhanced PRET efficiency has also been demonstrated for high aspect ratio nanorods which exhibit longer dephasing times than nanospheres, up to ~20 fs vs. ~5 fs for spheres.[120–122] The slow dephasing in nanorods is attributable to reduced radiative damping as a result of low energy LSPR, and the ~1.8 eV threshold for interband transitions.[63,122]

Plasmonic enhancement in solar devices by PRET often competes with FRET, which takes away excited carriers from the semiconductor, and hence distinction of the two processes is essential to preferentially enable PRET. In a recent work, Wu and co-workers differentiated the two processes and demonstrated that in the dipole–dipole coupling regime, exciting the plasmon results in coherent plasmon-to-semiconductor energy transfer via PRET, whereas exciting the semiconductor at its bandgap results in incoherent semiconductor-to-plasmon energy transfer via FRET (Fig. 8b).[87] They defined the efficiency

of dipole–dipole energy transfer for FRET (E_{FRET}) and PRET (E_{PRET}) as follows:

$$E_{FRET} = \frac{1}{1 + \left(\dfrac{R}{R_0}\right)^6} \tag{5}$$

$$E_{PRET} = \frac{\alpha_{semi}(\omega) + \alpha_{LSPR}(\omega) \cdot \left[\dfrac{1}{1 + \left(\dfrac{R}{R_0}\right)^6}\right]}{\alpha_{semi}(\omega)} \tag{6}$$

where R is the dipole–dipole separation distance, R_0 is the distance at which 50% of the energy is transferred, and α is frequency-dependent absorption coefficient. The PRET efficiency is dependent on the LSPR dephasing time where a slower plasmon dephasing (10 fs) than the semiconductor (5 fs) results in higher energy transfer via PRET, whereas longer semiconductor dephasing results in FRET. This indicates that when PRET dominates, FRET becomes less efficient and vice versa, conserving the total energy. The authors also demonstrated PRET efficiency as a function of the LSPR–semiconductor separation distance (Fig. 8c) where PRET is highest where the near-field of the metal nanostructure is the strongest, i.e. at minimum metal–semiconductor separation but not in direct physical contact. On the contrary, the distance dependence for FRET is inversely symmetric to PRET since the plasmons extract away the excited carriers from the semiconductor in the case of FRET.

While the evidence of PRET has been shown in solar photo-chemistry and photocatalysis, the contributions of PRET to enhance light trapping in MSCs remains poorly explored thus far. Since spectral overlap between metal and semiconductor is required for PRET, this mechanism occurs under similar conditions as radiative near field enhancement. Therefore, it is often difficult to differentiate the contributions of the radiative and non-radiative mechanisms. Further work is required to elucidate the potential for PRET in both DSSCs and PSCs.

3. Plasmon enhanced DSSCs

Since the first published report of metal nanostructure-mediated enhancement in dye-sensitized solar cells in 2000, advances in the fabrication of morphology-controlled metal nanostructures, and their subsequent implementation in DSSCs have resulted in significant efficiency enhancements.[123] In this section, we discuss the effects of shape, size, and composition of metal nanostructure on their ability to enhance light trapping in DSSCs, while summarizing recent progress in the field.

3.1 Influence of nanostructure size on DSSCs performance

The radiative and non-radiative plasmonic properties of metal nanostructures are largely controlled by their dimension, which strongly impacts their light harvesting capability. While nanostructures <90 nm in diameter are strong absorbers, larger nanostructures primarily scatter. The ratio of absorption to scattering as a function of size of Au nanospheres is depicted in Fig. 3a with the crossover point at 90 nm. Particularly in nanospheres, the absorption cross-section scales linearly with volume whereas scattering cross-section scales with the square of the nanosphere volume. At even smaller length scales, when the characteristic size is comparable to the electron mean free path (~20 nm for Au), these nanostructures display strong surface dispersion and electron–electron scattering.[107,124,125] A schematic illustration of the size-dependent enhancement mechanisms in DSSCs is shown in Fig. 9 where an Au nanosphere of variable size is in proximity of a sensitized TiO₂ nanoparticle. In the 5 nm size regime (Fig. 9a), where non-radiative effects are dominant, surface dispersion promotes photocharging

and hot-electron transfer (HET) from the metal to the semiconductor. At larger sizes radiative effects primarily drive light harvesting in DSSCs. At the 45 nm size regime (Fig. 9b), electromagnetic near-fields strongly contribute to plasmonic enhancement, whereas at 120 nm (Fig. 9c) far-field scattering dominates the increase in photocurrent.

Plasmon enhanced light harvesting in DSSCs has been achieved in two different configurations: (i) distribution of the metal nanostructures on top of the TiO₂ photoanode, and (ii) integrated within the mesoporous TiO₂ layer. In the former configuration, highly scattering >100 nm metal nanostructures are ideal to capture light not absorbed by the sensitizer and backscatter it into the active layer. Enhancement in this configuration is limited to far-field effects since the large separation between the metal/sensitizer and metal/TiO₂ limits HET, PRET, and near field enhancements. While enhancement schemes with metal nanostructures on top of the photoanode have been implemented,[126,127] the observed photocurrent improvements were comparable to incorporating a TiO₂ scattering layer, indicating this configuration does not require a plasmonic nanostructure. In a recent work, however, Taghavinia et al. used finite element method simulations of a nanoparticle/titania system and observed a 40% increase in absorption with 700 nm Ag microparticles relative to a 2% increase with 100 nm Ag nanoparticles.[128] This effect was attributed to the ability of the microparticles to divert light at larger angles, increasing the optical path length within the titania layer, thereby coupling light into more guided modes. Kang et al. also recently demonstrated that far field plasmonic enhancement can be achieved by incorporating nanostructures into the electrolyte layer.[21] The ~60 μm thickness of the electrolyte layer allows a larger density of nanostructures to be added, increasing the number of photons that can be scattered. By evaluating a range of diameters of Ag nanospheres from 8–98 nm, they observed a monotonic increase in efficiency with nanoparticle size. Maximum enhancements were achieved with highly scattering 98 nm nanoparticles.

In addition to the distribution of metal nanostructures on top of the photoanode, the best plasmonic enhancements in DSSCs have been achieved by homogeneous integration of nanostructures throughout the mesoporous TiO₂ active layer. In this configuration, nanostructures are in close proximity to
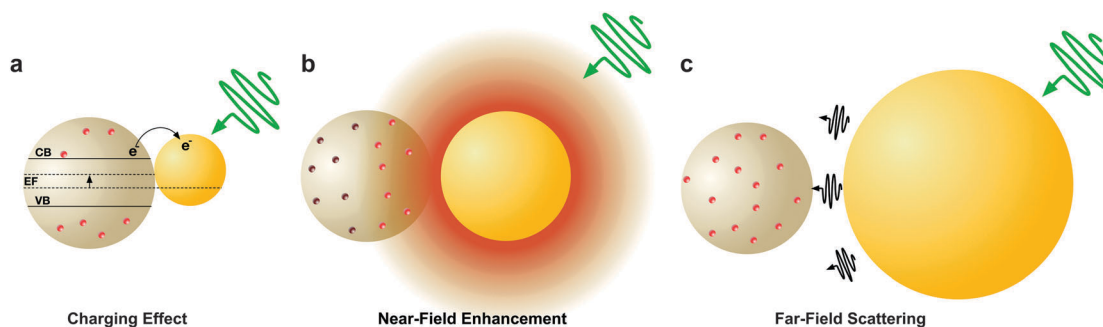

Fig. 9 Schematic illustration of the influence of the size of a nanostructure on the corresponding plasmonic enhancement mechanism. (a) The photocharging effect from a ~5 nm Au nanoparticle. (b) The near-field plasmonic effect from a ~45 nm Au nanoparticle. (c) Light scattering as a result of a ~120 nm Au nanoparticle.

both the TiO_2 and sensitizer molecules, enabling both radiative (near-field and far-field coupling) and non-radiative (PRET, HET) enhancements. Straightforward processing techniques and the versatility of the embedded configuration have enabled this architecture to be thoroughly studied; nanostructures in the range of 5–200 nm have been shown to successfully boost power conversion efficiency in DSSCs.[118,129,130] The impact of nanoparticle size in DSSCs has been studied by Wang *et al.* and Sardana *et al.*, who reported Au nanoparticles in the 30–50 nm range to be optimal for DSSC enhancement.[119,131] Incremental improvements in J_{sc} resulted from the presence of small (<5 nm) nanoparticles, however notable enhancements in V_{oc} were observed and attributed to photocharging effects, suggesting electron storage in ∼5 nm Au nanoparticles shifts the Fermi level of TiO_2 to more negative potentials.[118] The Fermi level shift results in longer electron lifetimes and higher recombination resistance, ultimately improving charge transport in the electrode, which is reflected in the increased V_{oc}. Medium sized (30–50 nm) Au nanostructures gave rise to the most dramatic improvement in J_{sc} and incident photon to charge carrier efficiency (IPCE), which is attributable to a combination of radiative and non-radiative effects. Both groups observed efficiency boost with larger nanoparticles (80–110 nm) where far-field scattering dominated other plasmonic enhancement mechanisms; however the champion efficiencies were achieved with 5–50 nm Au particles, although by different mechanisms.

3.2 Influence of nanostructure morphology

While early studies of plasmonic enhancement in DSSCs were focused primarily on spherical metal nanostructures,[23,27,133,134] recently anisotropic morphologies have gained tremendous attention due to their improved absorption and scattering properties, and enhanced spectral tunability.[51,66,67,78,130,132,135,136] Plasmonic enhancement in DSSCs has been observed with nanorods,[25,66] nanocubes,[30] nanoprisms,[51,135] and core/shell nanostructures,[25,30] among others. Non-spherical nanostructures with varying levels of symmetry give rise to enhanced polarizability. Increased polarizability results in multiple plasmon resonances including dipolar, quadrupolar, and higher order modes, as well as gives rise to red-shifts in the optical resonance.[59,137–139] These multiple plasmon modes facilitate spectral overlap and coupling with a range of dye sensitizers. Further, non-spherical nanostructures facilitate a higher concentration of charges localized at the corners and edges giving rise to confined near fields, attributable to the quasi-static lightning-rod effect discussed in Section 2.1.2.[39,80,82,84,85] Confined electromagnetic fields can be utilized as a secondary light source to augment absorption by proximal sensitizers.

A few examples of shape-controlled nanostructures employed in DSSCs and their respective absorption spectra and IPCEs are displayed in Fig. 10. Snaith and co-workers demonstrated one of the first works on plasmon-enhanced DSSCs with 15 nm spherical Au nanoparticles coated in a ∼3 nm layer of silica (Fig. 10ai) embedded in a 1.1 μm thick mesoporous TiO_2 layer. The nanoparticle plasmon resonance at ∼524 nm corresponded well with the Z907 sensitizer and improved the overall absorption of the

photoanodes (Fig. 10aii). They observed an increase of 57% in average device performance for plasmon-enhanced devices and an analogous improvement in the IPCE (Fig. 10aiii). They attributed the improvement in the nanoparticle incorporated devices to increased light harvesting as well as an increase in V_{oc} and FF correlating to the photocharging effect observed for small nanostructures discussed previously. Our group demonstrated the use of shape-controlled 45 nm edge-length Au nanocubes coated with a 5 nm silica layer, Au@SiO_2 nanocubes (Fig. 10bi). The optical resonance of the Au@SiO_2 nanocubes at 545 nm overlaps with the absorption peak of the N719 sensitizer at 530 nm. We performed finite difference time domain (FDTD) simulations showing the nanocube electric fields are localized near the edges and corners (Fig. 10bi-inset). We observed a 34% improvement in power conversion efficiency (PCE) using 1.8 wt% 45 nm Au@SiO_2 nanocubes, in agreement with the literature for this size and composition. The enhanced light harvesting by these shape-controlled nanostructures (relative to the spherical nanostructures in Fig. 10ai) is reflected in the IPCE spectra shown in Fig. 10biii. Contrary to the work described by Snaith and co-workers, we attributed the improved device efficiencies by the Au@SiO_2 nanocubes to radiative effects, resulting in plasmon-molecular coupling between the nanocubes and N719 dye; this is reflected in the increase in photocurrent with minimal change in V_{oc} or FF.
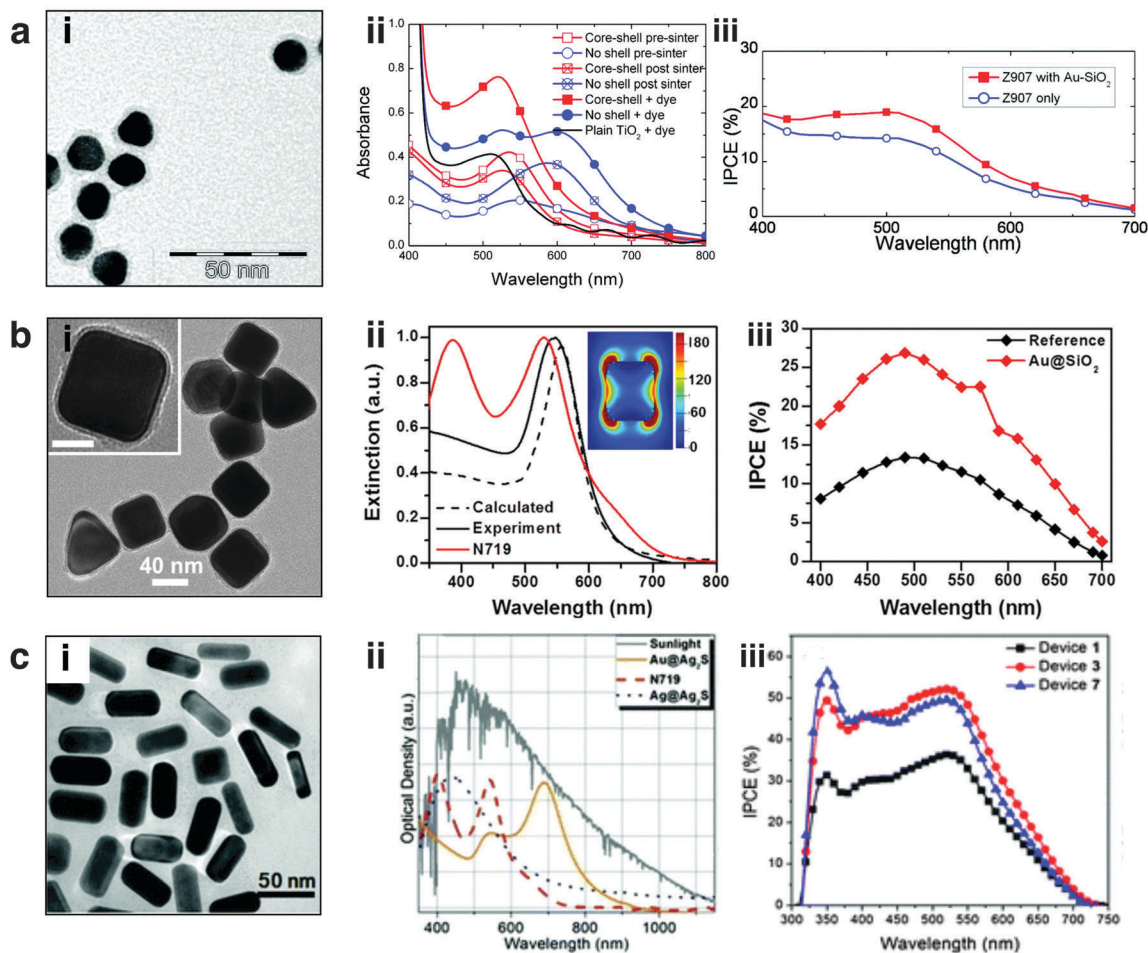
While Au nanospheres and nanocubes provide direct spectral overlap with the sensitizers used in DSSCs, modifying the morphology of the nanostructure, anisotropic nanostructures can achieve panchromatic light absorption. Chen *et al.* demonstrated this concept by using 50 nm Au nanorods (Fig. 10ci) with an aspect ratio of ∼2.2 and an Ag_2S protective coating embedded throughout the mesoporous TiO_2 active layer.[132] Nanorods support two distinct plasmon resonances, a transverse and a longitudinal mode; the longitudinal mode is tunable from the visible to near-IR by altering the aspect ratio of the nanorod. This is evident in Fig. 10cii, where the Au/Ag_2S nanorods show a longitudinal resonance at 685 nm enabling broadband solar light capture at wavelengths complimentary to N719 dye sensitizer. The authors observed a ∼38% increase in photocurrent generation in the 600–720 nm region as determined by IPCE (Fig. 10ciii), leading to an overall ∼30% enhancement in PCE by plasmon-enhanced devices.

Beyond the geometries discussed in Fig. 10, we have provided a comprehensive list in Table 1 including a range of shape-controlled metal nanostructures employed in DSSCs in recent literature. The diverse morphologies used for plasmonic enhanced MSCs demonstrate tremendous progress in this field in addition to providing motivation for further understanding of these metal/molecule systems.

3.3 Influence of nanostructure composition

The composition of metal nanostructures can also be varied to ensure successful coupling between plasmonic nanostructures and sensitizing molecules. The DSSC model system employs N719 dye, which has absorption bands centered at 395 nm and 535 nm. To maximize enhancement, a plasmonic nanostructure

Fig. 10 (a) (i) TEM image of Au@SiO$_2$ nanospheres, (ii) absorbance of active layers with and without particle incorporation, (iii) enhanced IPCE over the visible spectrum attributed to presence of Au nanoparticles. Adapted with permission from ref. 22. Copyright American Chemical Society 2011. (b) (i) TEM image of Au@SiO$_2$ nanocubes, (ii) extinction of calculated and experimental Au nanocubes overlaid with N719 absorbance; FDTD electric field profile is provided in the inset, colorbar represents $|E^2|/|E_0{}^2|$. (iii) IPCE of Au incorporated and control devices. Adapted with permission from ref. 78. Copyright American Chemical Society 2014. (c) (i) TEM of Au nanorods, (ii) extinction of Au@Ag$_2$S nanorods overlaid with N719 dye and solar irradiance, (iii) IPCE of control *versus* plasmonic devices. Adapted with permission from ref. 132. Copyright American Chemical Society 2012.

which supports dual resonances overlapping with the sensitizer is ideal, and can be achieved *via* dual-metal nanostructures. Experimentally, much work has been conducted studying the effects of dual-metal alloyed and core–shell nanostructures. This section will comparatively discuss the effect of monometallic and bimetallic nanostructures on light harvesting in MSCs.

3.3.1 Effect of monometallic nanostructures. The diverse literature on plasmon-enhanced MSCs have largely focused on the integration of monometallic Au[26,118,140,141] or Ag[21,72,135,142,143] nanostructures. Isotropic Au and Ag nanostructures have LSPRs located near 520 nm and 400 nm, respectively, allowing good overlap with at least one absorption peak of the N719 sensitizer, facilitating both radiative and non-radiative coupling. Broadband solar light absorption has also been achieved by incorporating anisotropic Au and Ag nanostructures, where each metal presents unique advantages. The high stability, facile synthesis, straightforward surface chemistry, and visible light capture of Au nanostructures have propelled their use in MSCs despite the high optical losses that result from interband transitions in the visible,

and intraband transitions (Drude losses) in the NIR.[144,145] Ag has low dielectric losses, dictated by the imaginary part of the dielectric function (see Section 2.1),[29,146] which results in stronger extinction coefficients and higher light scattering.[58,73] Despite the better radiative properties of Ag, champion plasmon-enhanced devices are similar for both Au and Ag, noting that the highest plasmon-enhanced PCE of 10% recorded thus far has been achieved with Au nanostructures.[28,118,133,144,146,155]

Notably, Al has recently been considered as a strong candidate for plasmonic enhancement in both photodetectors and photovoltaics due to its LSPR sensitivity to surrounding medium and broad spectral tunability between 350–500 nm.[147,148] With low optical losses and minimal plasmon damping, Al nanoparticles are expected to have higher light scattering efficiency than both Au and Ag in the visible.[149,150] Huang and co-workers demonstrated a near 13% increase in device efficiency with the incorporation of 50 nm Al nanospheres.[151] While the light trapping abilities of Au and Ag have been shown to be superior to Al at similar particle densities, Al nanostructures offer other

This journal is © The Royal Society of Chemistry 2016

Energy Environ. Sci., 2016, **9**, 1577–1601 | **1587**

Table 1 A summary of metal nanostructures utilized in DSSCs to improve their power conversion efficiencies (PCE). The nanostructure composition, shape, and size are highlighted and corresponding performance of reference and plasmon-enhanced devices is given

Composition	Passivation layer	Nanostructure	Size (nm)	Reference PCE (%)	Plasmon enhanced (%)	Enhancement (%)	Ref.
Ag	EMIm-DCA	Nanosphere	8–98	6.34	8.05	27	21
Au	TiO_2	Nanosphere	100	5.21	5.97	15	228
Au	SiO_2	Nanosphere	15	1.70	4.00	135	22
Au	—	Nanosphere	15	6.52	7.70	18	229
Au	—	Nanosphere	36	6.17	7.35	19	131
Au	—	Nanosphere	18	3.44	4.11	19	229
Au	Ag_2S	Nanorod	40	5.80	7.10	22	132
Au	SiO_2/TiO_2	Nanoparticle	5	9.29	10.21	10	118
Au	TiO_2	Nanosphere	20	6.03	8.46	40	23
Au/Ag	TiO_2	Nanosphere	15	8.30	10.80	30	133
Ag	—	Nanodome array	300	5.64	5.93	5	157
Ag	SiO_2	Nanoparticle	<5	2.70	4.00	48	24
Ag	SiO_2	Nanoparticle	<5	6.20	8.10	31	230
Au@Ag	—	Nanorod	70	5.91	8.43	43	25
Ag	TiO_2	Nanowire	80 nm	6.16	8.84	44	66
Ag	—	Nanoparticle	<5	6.98	8.19	17	151
Au	TiO_2	Nanoparticle	5	6.25	8.13	30	26
Au	SiO_2	Nanoprism	20–150	3.90	4.50	15	51
Ag	SiO_2	Nanoprism	30	6.50	8.40	29	135
SiO_2@AuNP	TiO_2	Nanosphere	200	4.51	5.74	27	27
Ag	TiO_2	Nanoparticle	<5	7.10	8.90	25	142
Ag	—	Square array	500	4.59	5.69	24	68
Au	DMAP	Nanoparticle	5	3.89	4.34	12	182
Ag	—	Nanoplatelet	20	8.60	10.10	17	67
Ag	—	Nanoparticle	2–4	2.57	4.86	89	231
Ag	—	Nanoparticle	2–4	2.57	8.15	217	70
Ag	—	Nanoparticle	100–300	1.43	3.01	110	71
Ag	—	Nanoparticle	50–100	1.44	1.96	37	72
Au	TiO_2	Nanooctrahedron	25	6.00	7.38	23	136
Au	—	Nanoparticle	<5	5.00	6.00	20	177
Au	—	Nanosphere	100	2.70	3.30	22	129
Au	—	Nanoparticle	<5	6.76	7.77	15	155
Au	—	Nanoisland	9	5.73	6.95	21	141
Au	—	Nanoparticle	<5	4.34	5.52	27	156
Ag	—	Nanoparticle	<5	5.40	6.90	28	232
Ag	TiO_2	Nanosphere	20	7.80	9.00	15	143
Ag	—	Nanosphere	20	5.80	7.04	21	233
Ag	TiO_2	Nanosphere	30–80	5.29	6.23	18	178
Au	SiO_2@TiO_2	Nanosphere	20	3.07	6.42	109	134
Au	SiO_2	Nanosphere	15	2.00	2.30	15	183
Ag	TiO_2	Nanosphere	5	9.59	10.80	13	119
Au/Ag	—	Composite	—	6.23	7.51	21	234
Au	SiO_2	Nanosphere	30–160	1.94	2.66	37	28
Al	—	Nanosphere	50	6.15	6.95	13	151
Au–Ag alloy	—	Amorphous	180	5.94	7.85	32	130
Au	PVP	Nanosphere	20	3.30	4.30	30	235
Au	—	Planar electrode	—	6.00	7.00	17	160
Au@Ag	TiO_2	Nanosphere	25	7.80	9.70	24	29
Au	SiO_2	Nanocube	45	5.80	7.80	34	78
Ag	TiO_2	Nanosphere	5	1.42	1.83	29	180
Au	TiO_2	Nanorod	90	6.22	7.05	13	219

unique advantages.[151,152] The few nanometer native oxide on Al nanostructures surface provides better chemical stability toward the corrosive liquid electrolytes employed in DSSCs without the need for further surface passivation. Unlike Au and Ag, the work function of Al (4.06 eV) lies below that of TiO_2 (4.26 eV), therefore the anticipated quenching via charge transfer from TiO_2 to metal nanoparticles and carrier recombination at high particle concentrations are significantly reduced by using Al. The benefit of the low work function of Al was demonstrated experimentally using impedance spectroscopy, which revealed that the addition of the Al nanostructures improved electron transport and increased carrier lifetimes relative to control devices.

The authors proposed the utility of bimetallic core/shell (Au or Ag core/Al shell) architectures to tailor nanostructures with dual functionalities – strong light trapping and suppressed recombination with increased stability.

3.3.2 Effect of bimetallic nanostructures. Bimetallic nanostructures, as briefly discussed in the previous section, synergistically integrate two metals with complementary properties either in core/shell architecture or mixed alloy to generate superior properties not achieved with either metal alone. Suh and co-workers used a double layer approach, where two layers of mesoporous TiO_2 containing ~29 nm Ag nanospheres and ~33 nm Au nanospheres, respectively, were deposited.[153]
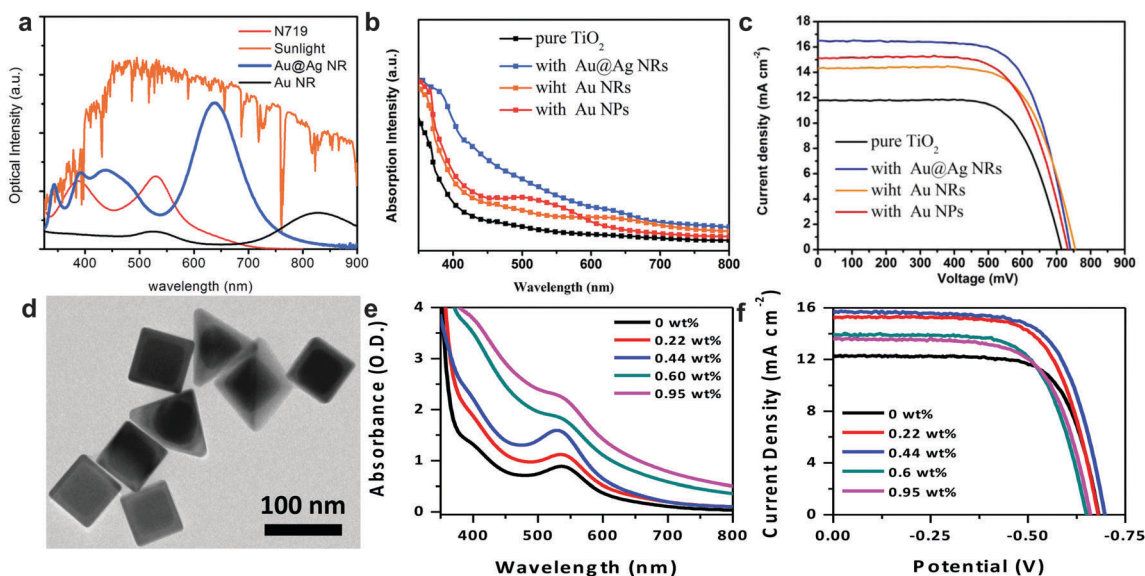
The presence of both metals in the device enabled both energy matching and near field coupling with both peaks of the N719 sensitizer. The best plasmon-enhanced device achieved an efficiency of 10%, nearly 20% higher than the reference without the need for complex nanoparticle synthesis. The dual nanoparticle approach discussed here requires multiple layers, thus requiring a relatively thick active layer and subsequent high bulk recombination. To overcome this limitation, bimetallic architectures incorporating two metals into a single nanostructure have been of significant interest.

Huang and co-workers reported the incorporation of ∼200 nm Au/Ag alloy popcorn nanoparticles in DSSCs.[130] The irregular shape of the nanoparticles gave rise to broadband absorption spanning from the UV to the NIR of the solar spectrum. This broadband absorption led to a 16% improvement in efficiency with 2.38 wt% of nanoparticles in the active layer. Despite the enhancement, impedance spectroscopy revealed that the incorporation of such large and irregularly shaped nanoparticles increased the series resistance and charge transfer resistance in the devices.

Recently, Jiao and co-workers utilized Au@Ag core@shell bimetallic nanorods (Fig. 11a) in DSSCs and demonstrated that the addition of the Ag layer around the Au nanorod core increased the extinction of the nanostructure.[25] The bimetallic nanorods enabled spectral overlap with the 535 nm absorption peak of N719, enhancing light harvesting in the visible, as well as capturing NIR light which the sensitizer does not absorb (Fig. 11b). The bimetallic nanorods increased the PCE by ∼43% with 3.68 wt% of particle density (Fig. 11c). Our group recently demonstrated the use of hybrid bimetallic Au core/Ag shell nanostructures with dual shapes – nanocubes and nanopyramids

(Fig. 11d and 1e).[30] Dual shapes were dictated by the Au core geometry where the bimetallic nanocubes emerged from rounded-corner nanocube cores and bimetallic nanopyramids emerged from the truncated Au nanocube cores.[41] The dual shapes and bimetallic composition gave rise to two distinct dipolar resonances at 530 nm, attributable to the nanocubes, and at 630 nm, attributable to the longitudinal modes of the pyramids (see Fig. 1b). These bimetallic nanostructures directly overlap with the absorption peaks of N719 sensitizer, giving rise to enhanced light scattering and near-field enhancements, and simultaneously absorbing light complementary to the sensitizer absorption, giving rise to broadband light harvesting in the DSSCs. The particle densities of the nanostructures were varied and a systematic increase in light absorption (Fig. 11e) and corresponding trends in photocurrent density (Fig. 11f) were observed. The bimetallic nanostructure resulted in a 27% improvement in DSSC efficiency and was achieved with a nominal 0.44 wt% particle density. This ∼6× decrease in particle density suggests hybrid bimetallic nanostructures have the potential to ultimately achieve high efficiency thin film DSSCs with low materials and processing costs.

3.3.3 Effect of the capping layer composition. For successful integration of metal nanostructures in MSCs, surface passivation of the nanostructures is necessary. This protective capping layer serves multiple purposes: (1) provides thermal stability during the high temperature annealing of the photoanodes, (2) provides chemical stability from corrosive liquid electrolytes, and (3) minimizes carrier recombination on the metal surface. Silica (SiO_2) and titania (TiO_2) are the most commonly employed capping materials chosen due to the straightforward synthesis which gives rise to homogeneous thin (3–5 nm) layers

Fig. 11 (a) Solar irradiance and extinction of Au nanorods and Au@Ag nanorods. (b) Absorption of TiO_2 electrodes with Au@Ag nanoparticles incorporated. (c) Current–potential scans of plasmonic particle incorporated and control DSSCs. Panels a–c adapted with permission from ref. 25. Copyright Royal Society of Chemistry 2015. (d) TEM image of Au@Ag nanostructures designed by our group. (e) Extinction of TiO_2 anodes with incorporated Au@Ag nanostructures. (f) Current–potential scans of Au@Ag nanostructure incorporated DSSCs. Panels d–f adapted with permission from ref. 30. Copyright American Chemical Society 2016.

This journal is © The Royal Society of Chemistry 2016

Energy Environ. Sci., 2016, **9**, 1577–1601 | **1589**

with minimal alteration to the optical properties of the metal nanostructure.[154] The composition of the capping layers can drive or block different plasmonic enhancement mechanisms. A conductive TiO_2 layer enables charge accumulation and transfer of hot carriers that are generated following photoexcitation from the metal nanostructures to the mesoporous active layer.[143] Alternatively, silica provides good thermal and chemical stability but does not allow hot electrons to transfer over the Schottky barrier unless the thickness of the SiO_2 layer is less than its tunneling barrier height (~ 3 nm).[78,106] Because insulating coatings forgo electronic effects, the photovoltage is typically unaffected and enhancement effects are attributed to increased photocurrent, while both photocurrent and photovoltage increase with semiconducting coatings.[118,119] An impactful work by Kamat and co-workers revealed intriguing results when SiO_2 and TiO_2 capping layers were compared in DSSCs.[118] The authors encapsulated 5 nm Au nanospheres with SiO_2 or TiO_2, and incorporated similar particle densities in DSSCs. They observed the TiO_2 capping layer weakens plasmonic light trapping modes while giving rise to enhanced photocharging. The semiconducting behavior of TiO_2 enables electron storage within the metal nanostructure core, resulting in Fermi level equilibration and shifting the surrounding mesoporous TiO_2 matrix to a more negative potential. Enhancements from the TiO_2-capped particles stem from increased open circuit voltage in the device, while SiO_2 capped particles show minimal impact on V_{oc} but exhibit a marked increase in J_{sc}, suggesting that enhancements are attributable to enhanced light trapping.[118]

In addition to their role as capping layers, SiO_2 and TiO_2 have been employed as "nanocarriers" loaded with metal nanoparticles or used to generate multilayered core/shell architectures to achieve broadband absorption. Both SiO_2 and TiO_2 nanospheres loaded with Au and/or Ag nanoparticles have been reported resulting in $>20\%$ improvement in device efficiencies.[29,67,155,156] In a unique work by Belcher and co-workers, multilayered TiO_2/Au/TiO_2 core/shell/shell spherical nanostructures were designed by wet chemical approaches (Fig. 12a). The authors observed that relative to the Au/TiO_2 core/shell nanostructures, multilayered geometries enabled highly tunable broadband plasmon resonances resulting in a range of colors and panochromatic photon absorption (Fig. 12b and c).[133]

By modifying the metal composition (Au or Ag) or altering the thickness of the TiO_2 layer plasmonic coupling was extended from near-UV to near-IR. The enhanced tunability of the multilayered "nanoshell" architecture can be understood from the plasmon hybridization model where the core and shell plasmons hybridize to give rise to bonding (bright modes) and antibonding (dark modes). The core to shell ratio determines the energy level splitting between the two modes: a larger splitting results in greater tunability as well as higher sensitivity to the dielectric constant of the surrounding medium. These properties collectively allowed tunability of the multilayered TiO_2/Au/TiO_2 nanostructures to the near-infrared. The best performing plasmon-enhanced DSSCs resulted in a 10.8% PCE, which is the highest reported to date.

3.4 Plasmonic nanostructures fabricated by top-down approaches

While the majority of plasmon-enhanced DSSCs reported in the literature have employed wet-chemically synthesized colloidal metal nanoparticles, a number of studies have featured top down fabrication approaches in the design of plasmonic components. Long range nanostructures which support propagating surface plasmon polaritons (SPPs) have been fabricated *via* nanoimprint lithography,[68,157] electron beam lithography (EBL),[158,159] and colloidal lithography.[160] Analogous to LSPRs, SPPs undergo radiative and non-radiative relaxation mechanisms discussed in Section 2, where the field enhancements can effectively extend up to 1 µm into adjacent dielectric.[158,161]

One of the simplest approaches to implement centimeter-scale plasmonic nanostructures into MSCs is through nanoimprint lithography, in which patterns are imprinted into the mesoporous structure with inverted templates and subsequently filled with metal *via* evaporation or chemical reduction. McGehee and co-workers used a quartz template to imprint an array of hemispherical wells onto a mesoporous TiO_2 substrate and subsequently thermally deposited an Ag cathode that functioned as a nanopatterned plasmonic rear reflector (Fig. 13a).[157] The SPP modes generated in these DSSCs enhance light trapping *via* near field enhancement due to propagating SPPs and scattering from ~ 300 nm hemispherical Ag wells. The authors showed calculated enhancement of energy density in the active layer
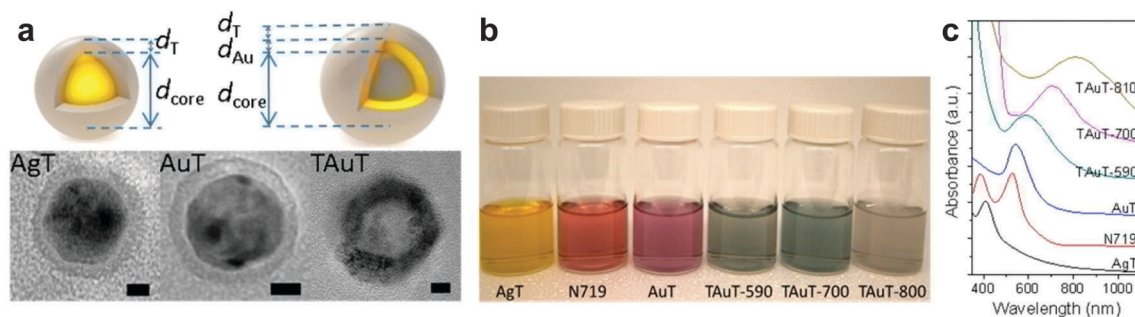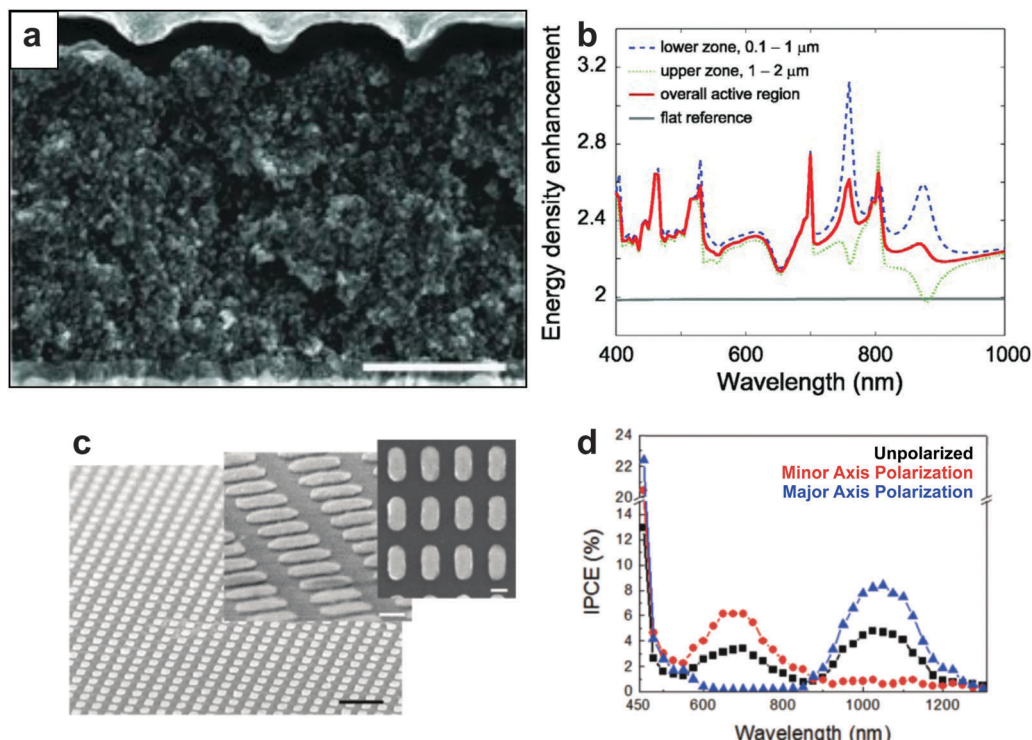

Fig. 12 (a) Schematic and TEM of Ag@TiO$_2$, Au@TiO$_2$ and TiO$_2$@Au@TiO$_2$ core−shell nanoparticles, (scale bar = 5 nm). (b) Optical images demonstrating macroscopic color tunability of core−shell nanoparticles. (c) Extinction spectra of core−shell nanostructures corresponding to different sizes and compositions. Figure adapted with permission from ref. 133. Copyright American Chemical Society 2013.

1590 | *Energy Environ. Sci.*, 2016, **9**, 1577−1601

This journal is © The Royal Society of Chemistry 2016

Fig. 13 (a) Cross sectional scanning electron micrograph of solid state DSSC with plasmonic nanodome array (scale bar = 1 µm). (b) Calculated energy density enhancement over visible and NIR wavelength ranges. Panels a and b adapted with permission ref. 157. Copyright John Wiley and Sons 2011. (c) Scanning electron micrographs of lithographically fabricated Au nanorods (black scale bar = 500 nm; white scale bar = 100 nm). (d) Incident photon to current efficiency for devices with unpolarized, minor, and major axis polarization. Panels c and d adapted with permission from ref. 159. Copyright American Chemical Society 2010.

(Fig. 13b) in the lower region (near-field effects) and upper region (scattering), which correlated well with experimental results and overall enhancements observed in the active layer. Further, EBL has also been employed for the fabrication of highly uniform plasmonic nanoarrays to study the interactions between plasmons and TiO_2 MSCs. Misawa et al. fabricated a rectangular array of elliptical nanoparticles on a planar TiO_2 surface, as shown in Fig. 13c.[159] The lack of spectral overlap between the TiO_2 substrate and the LSPR implicates that radiative effects and PRET do not play a role in the observed enhancements, indicating that hot carrier transfer allows the plasmonic nanostructures to act as a direct sensitizer to the TiO_2. Elliptical nanoparticles support both transverse and longitudinal plasmon modes; each mode can be individually excited with parallel or perpendicular polarized incident light, respectively. The authors activated distinct plasmon modes by polarized light, and subsequent charge generation in TiO_2 was observed at either the longitudinal mode or transverse mode as evident in the incident photon to charge carrier efficiency spectra (Fig. 13d). In a similar study, Hägglund et al. enhanced the performance of DSSCs with nanofabricated elliptical gold disks and demonstrated improved efficiency.[158]

Ding et al. used nanoimprint lithography to pattern a square grid into the TiO_2 active layer and subsequently filled it with Ag, resulting in a ∼25% enhancement in PCE.[68] The authors attribute the enhancement to both plasmonic effects resulting from propagating SPPs facilitated by the periodic Ag array and improved charge transport properties resulting from improved conduction between the TiO_2 nanoparticles and increased interfacial area. In another work, Jiang et al. designed a topologically ordered Au counter electrode by first depositing a layer of close packed polystyrene spheres and evaporating Au onto the surface leaving an ordered long range array of Au.[160] The authors demonstrated ∼18% increase in PCE, attributed to increased light scattering and subsequent light trapping which was evident from the increased broadband absorption, IPCE, and J_{sc}.

Top-down approaches are typically not cost-effective for large scale implementation, involve time-consuming processing techniques, and are ineffective in uniformly integrating metal nanostructures throughout the mesoporous active layer. However, top down approaches do provide precise location and orientation of the plasmonic nanostructures and cleaner interfaces with the TiO_2 active layer. This enables researchers to perform fundamental studies that will probe the mechanisms of enhancement in MSCs without variations in particle densities or local variations in interparticle distances within the mesoporous layer.

4. Plasmon enhanced perovskite solar cells

Mesoporous perovskite solar cells (PSCs) have diverged rapidly from their predecessors, DSSCs, since 2011. The projected

This journal is © The Royal Society of Chemistry 2016

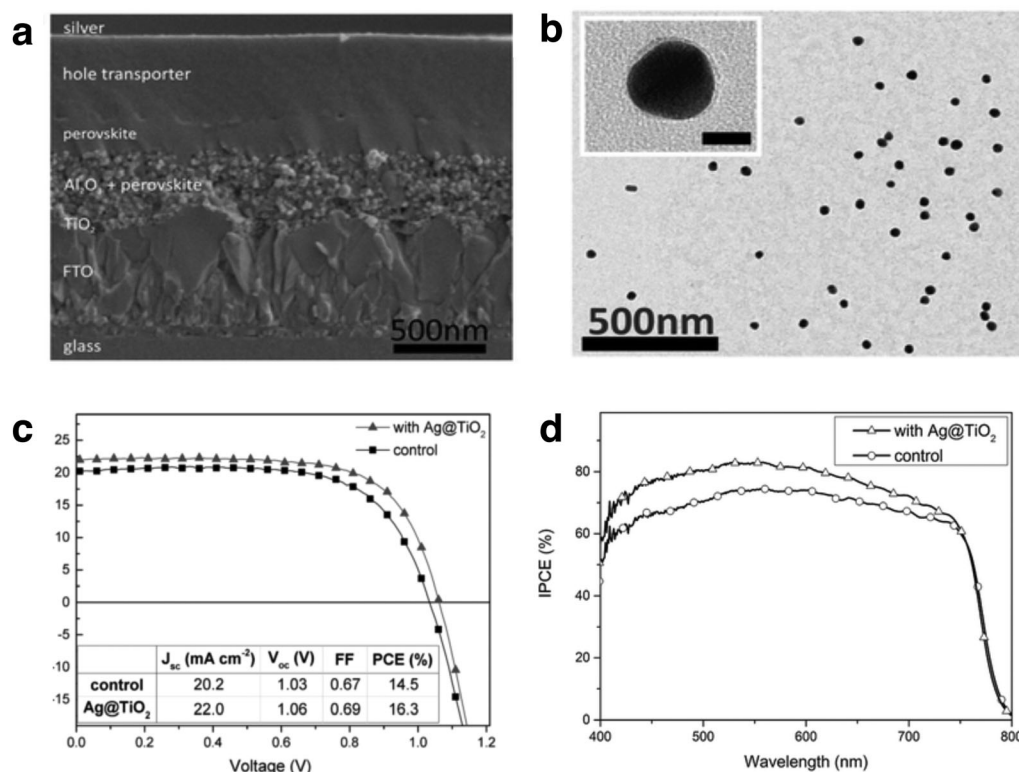Energy Environ. Sci., 2016, 9, 1577–1601 | 1591

power conversion efficiency (PCE) of PSCs match those of crystalline Si solar cells. A steep increase in PCE has been observed in methylammonium lead halide (MAPbX$_3$, X = Br, Cl, I) perovskites and recently there has been significant interest in using plasmonic enhancement to improve the performance to reach or even surpass the Shockley–Queisser limit. The underlying mechanisms of enhancement are similar to those discussed in Section 2; however, it has been proposed that the presence of LSPRs decreases the exciton binding energy within the perovskite absorber, resulting in higher internal efficiency.[162]

The earliest demonstration of plasmonic enhancement in PSCs was published in 2013 by Snaith and co-workers.[162] They mixed SiO$_2$ coated Au nanoparticles into mesoporous Al$_2$O$_3$ scaffold, which improved the photocurrent density by 14.5% with minimal changes in the V_{oc} and FF. The authors correlated the observed enhancement in device performance to a three-fold reduction in exciton binding energy (E_B) of the perovskite in the presence of Ag LSPR, as evidenced by photoluminescence. A decrease in E_B at the perovskite/metal interface has also been calculated by Wu and co-workers using 3D FDTD simulations, demonstrating that the exciton binding energy in CH$_3$NH$_3$PbI$_3$ is reduced in the presence of copper nanoparticles.[163] In another recent study, Snaith and co-workers demonstrated significant spectral enhancement when TiO$_2$ coated Ag nanospheres were embedded in mesoporous Al$_2$O$_3$/perovskite active layer, boosting the measured device efficiencies by ~20%, with a champion efficiency of 16.3% (Fig. 14a–c).[164] Surprisingly, IPCE measurements

revealed broadband enhancement over the entire absorption spectrum, rather than in the spectral region of the Ag nanoparticle LSPR (Fig. 14d). The observed enhancement was not correlated to reduction in E_B but attributed to the presence of highly polarizable nanoparticles, which improve the radiative decay of excitons and enhance the reabsorption of emitted radiation. This gives rise to increased optical path lengths through light scattering.[164] In another study, irregular Au–Ag alloy nanoparticles with a broad resonance peak between 370–800 nm were inserted into a mesoporous TiO$_2$ layer, resulting in a 15.7% increase in PCE.[165] Improvements in V_{oc} and FF were attributed to rapid injection of electrons into TiO$_2$, verified by a quenching of photoluminescence lifetimes in the presence of metal NPs.

Beyond mesoporous architectures, PSCs have also been fabricated in planar geometries, which function much like p–i–n junction solar cells, where the intrinsic layer is the perovskite. Recent efforts in plasmonic enhancement of planar perovskites have shown promising avenues to boost the efficiency and improve charge transport. Sun and co-workers sandwiched Au nanoparticles between two layers of low temperature-processed TiO$_x$ film and observed enhanced photocurrent density and external quantum efficiency (EQE).[165] The authors attributed the effect to hot electron injection from the plasmonic nanoparticles filling the trap states of TiO$_x$, leading to increased charge carrier density and improved mobility. The group also performed scanning Kelvin probe microscopy, which showed that Au nanoparticles lowered the work function of TiO$_x$ and

Fig. 14   (a) Cross-sectional scanning electron micrograph of a mesoporous perovskite solar cell. (b) TEM image of Ag@TiO$_2$ (inset scale bar = 20 nm). (c) Current–potential scan of control and plasmon-enhanced PSCs. (d) IPCE of control and plasmon enhanced PSCs, indicating broad spectral enhancement with the presence of Ag@TiO$_2$ nanostructures. Figure adapted with permission from ref. 164. Copyright John Wiley and Sons 2015.

1592 | Energy Environ. Sci., 2016, 9, 1577–1601

This journal is © The Royal Society of Chemistry 2016

correlated well with the improved V_{oc} in their device performance. Hsu *et al.* recently compared prismatic silver nanostructures of different sizes and found that the near-infrared resonant (~ 700 nm) prisms demonstrated the greatest improvements in PCE, EQE, and J_{sc} (up to 12% improvement).[52] This was likely due to the ability of the nanoprisms to capture light complementary to the MAPbI$_{3-x}$Cl$_x$ perovskites, resulting in broadband light trapping. Mixed halide, MAPbI$_{3-x}$Cl$_x$, perovskite was also used in a recent study where Ag nanoparticles resonant at ~ 427 nm were embedded in a PEDOT:PSS hole transport material and interfaced with the perovskite.[166] The improved J_{sc} was attributed to improved hole extraction through the nanoparticles. By a different mechanism, Yan *et al.* showed that scattering from nanostructured Au electrode improves light capture in the NIR and increases the optical path length of the perovskite active layer.[167]

Plasmonic enhancement of PSCs has made tremendous strides in only a few years, but many mechanistic questions remain unexplored and would be of significant interest for further study. For example, in a recent work 3D FDTD simulations were performed on nanosphere/perovskite systems, yielding 6–12% absorption enhancement depending on perovskite film thickness.[168] This may constitute a theoretical absorption limit, as the study included unusually high particle density (10% as opposed to ~ 1% by volume typically used in experiments) and neglects potential negative effects on charge transport by the additional nanoparticles. Furthermore, the spontaneous polarization of perovskite crystals adds both complexity and potential for energy harvesting. This behavior of perovskites not only impacts the type of metal nanostructures used (shape, size, composition control), but also their precise location with respect to the perovskite.[169] Baumberg and co-workers recently showed that excitons in 2D organic–inorganic perovskites interact with selective SPP modes of metal nanogratings at specific angles of incident light to produce paired quasiparticles termed "image biexcitons".[170] They showed the exciton mode is spectrally split by Coulomb coupling with its image in the metallic mirror, indicating that controlling the position and polarization of metallic nanosurfaces provides avenues for strong light-matter interactions at the metal/perovskite interface. Beyond coupling metal nanostructures with perovskites, recent evidence also suggests intrinsic plasmonic effects exist within perovskites with quantum confinement in 2D or 3D nanostructures.[171] Deeper understanding of the fundamental interactions between plasmonic nanostructures and polarizable perovskites could lead to future optimization of both the light harvesting abilities and charge transport mechanisms in PSCs.[166]

5. Spectroscopic analyses of fundamental processes

Time-resolved spectroscopic techniques including pump–probe transient absorption spectroscopy (TAS) and time-resolved photoluminescence (TrPL) are powerful approaches to probe and understand fundamental processes occurring in solar cells.[172]

These spectral techniques enable us to identify and decouple the mechanisms of carrier generation, charge separation, transport, and recombination at various interfaces in MSCs. The use of these techniques is especially critical because, in addition to improving the carrier density, the presence of metal nanostructures also gives rise to other complex phenomena that simultaneously occur in MSCs. In this section, we will summarize the progress made thus far in understanding plasmon-enhanced phenomena in both DSSCs and PSCs with TAS and TrPL. Snaith and co-workers demonstrated one of the first studies on the use of femtosecond spectroscopy to understand the impact of metal nanoparticles in MSCs.[22] They performed TAS to probe the effect of 15 nm Au@SiO$_2$ nanoparticles incorporated in DSSCs sensitized with Z907 dye and observed an increase in amplitude of transient absorption in the presence of nanoparticles (Fig. 15a). They attributed this observation to an improvement in photobleaching signal of the dye due to higher molecular absorption coefficient (ε) of Au nanoparticles relative to the sensitizer. The ε of 15 nm Au nanoparticles is $\sim 10^9$–10^{10} M^{-1} cm^{-1},[173] whereas that of Z907 is $\sim 10^4$ M^{-1} cm^{-1}. The authors measured the decay kinetics of the photobleaching band at 520 nm and obtained a lifetime of 5 ps, which correlated well with the known electron–phonon relaxation time of ~ 3 ps for 15 nm Au nanoparticles. They attributed this fast decay to the relaxation of the hot electron population and further suggested that plasmonic enhancement of photocurrent can only occur if the photoexcited dye transfers carriers into TiO$_2$ in the first tens of femtoseconds before the decoherence of plasmons occurs.

Our group recently demonstrated plasmonic enhancement in DSSCs sensitized with N719 with Au core/Ag shell bimetallic nanostructures, Au@Ag NSs (see Fig. 1e and 11d). We varied the particle density of Au@Ag NSs in DSSCs and examined the dynamics with TAS.[30] Due to the strong spectral overlap between Au@Ag NSs (see Fig. 1b) and N719, the observed photobleaching band at 530 nm had contributions from both the photobleaching of the dye and relaxation of the plasmons (Fig. 15c). A correlation between TAS evolutionary spectra and particle density is evident within 1 ps of transient decay. A biexponential fit to the transient decay gave two distinct lifetimes, which we attributed τ_1 to electron injection into the conduction band of the TiO$_2$ from the singlet metal to ligand charge transfer (^{1}MLCT) states and τ_2 to the triplet (^{3}MLCT) states of the excited N719 complexes.[174] An increase in amplitude of the decay kinetics was observed for photoanodes embedded with nanostructures, similar to those observed by Snaith and co-workers; the amplitude monotonically increased with particle density (Fig. 15d). We also correlated this to stronger ε of metal nanostructures relative to N719, which is 1.58×10^4 M^{-1} cm^{-1}.[175] Further, our amplitude-weighted lifetime, τ_{avg}, drastically decreased with increasing particle density relative to the reference sample, indicating that Au@Ag NSs improved the light trapping and further enhanced e$^-$/h$^+$ pairs generated in the DSSCs. This gives rise to more carriers being available to transfer to the TiO$_2$ conduction band and faster injection before recombination can occur. The fast carrier injection results in shorter exciton lifetimes.
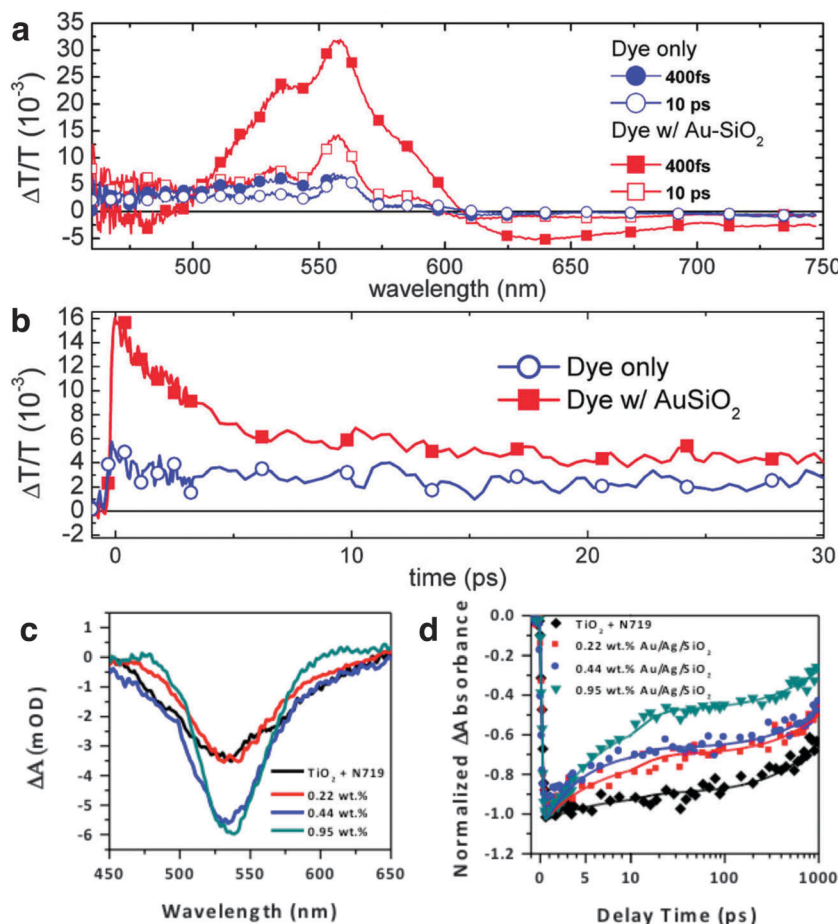
Fig. 15 (a) Change in absorption for plasmon-enhanced and control devices 10 ps after excitation. (b) Transient decay profiles of devices at 520 nm with 555 nm excitation. Panels a and b adapted with permission from ref. 22. Copyright American Chemical Society 2011. (c) Transient decay profile pumped at 400 nm and probed at 530 nm of N719 sensitized reference, and plasmon-enhanced DSSC photoanodes with 0.22 wt%, 0.44 wt%, and 0.95 wt% bimetallic Au/Ag nanostructures. The spectra were measured at 1 ps time delay. (d) Decay kinetics at 530 nm for all samples shown in c. All decay kinetics are shown with experimental data (symbols) fitted with a biexponential decay function (smooth line). Panels c and d adapted with permission from ref. 30. Copyright American Chemical Society 2016.

The mechanisms of plasmonic enhancement have also recently been investigated in PSCs by Zhao and co-workers with steady-state photoluminescence and TrPL.[162] The authors compared $CH_3NH_3PbI_{3-x}Cl_x$-based PSCs with and without 80 nm $Au@SiO_2$ nanoparticles and observed a significant decrease in steady-state PL (Fig. 16a), and faster decay in TrPL (Fig. 16b) in the presence of the nanoparticles. Further, by comparing PL as a function of temperature for the reference and plasmon-enhanced samples, the authors observed rapid PL quenching with increasing temperature for the samples with $Au@SiO_2$ nanoparticles embedded (Fig. 16c and d). They attributed this phenomenon to a decrease in exciton binding energy (E_B) which dropped from 98 meV for the control to 35 meV for the plasmon-enhanced samples. However, more recently the same authors described that for perovskites with already low E_B, such as $MAPbI_3$ (10 meV), metal nanoparticles do not appreciably decrease the E_B but rather enhance the optical path length by reabsorption of exciton radiation.[164] Yuan *et al.* also observed a significant decrease in steady-state PL and shorter TrPL lifetimes in $MAPbI_3$ based PSCs embedded with Au–Ag alloy
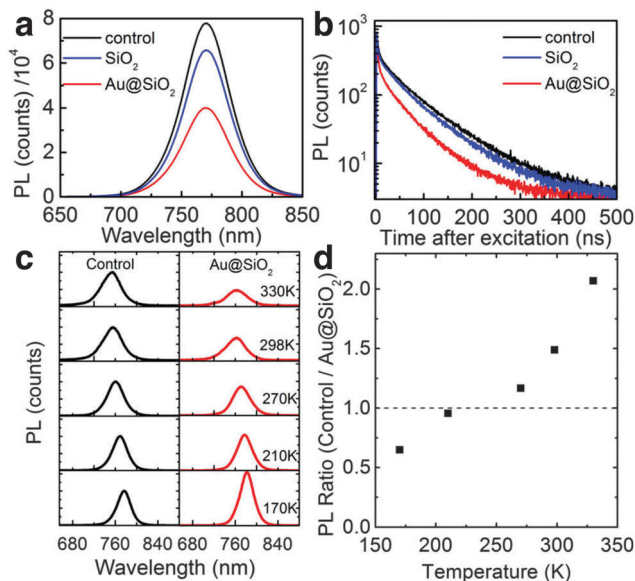
popcorn nanoparticles.[165] They attributed the observed trends to faster charge transfer at the metal/semiconductor interface, resulting in the suppression of charge recombination.

Despite the tremendous rise in metal-enhanced MSCs, few studies have used time-resolved spectral techniques to probe fundamental dynamics and understand the foundational principles of plasmonic enhancement. Spectroscopic investigation in both DSSCs and PSCs is necessary comparing the size, shape, and composition effects of plasmonic nanostructures, and the thickness and nature of the surface capping layer (SiO_2 *vs.* TiO_2 coating) to decouple the mechanisms of PRET, HET, and radiative plasmonic enhancements.

6. Challenges in plasmonic device fabrication

While the past decade has witnessed a promising rise in plasmonic enhancement of solar cells and successful improvements in device efficiencies, several challenges remain both in fabrication

Fig. 16 (a) Time-integrated photoluminescence data. (b) Time-resolved photoluminescence decays at 765 nm for perovskite only Al$_2$O$_3$ samples, Au@SiO$_2$ incorporated samples, and SiO$_2$ incorporated samples. (c) Temperature dependent time-integrated photoluminescence of control and Au@SiO$_2$ samples. (d) Ratio of integrated photoluminescence for the control to Au@SiO$_2$ samples. Figure adapted with permission from ref. 162. Copyright American Chemical Society 2013.

of metal nanostructure integrated devices and understanding fundamental phenomena at the metal/sensitizer or metal/semiconductor interface. This section will provide an account of the challenges in this research area and possible ways to surmount these challenges. When metal nanostructures are integrated in DSSCs and PSCs, the optical enhancements must outweigh detrimental electronic and electrochemical effects that arise from (i) recombination of electron–hole pairs on the metal surface, (ii) degradation of the metal during the high temperature annealing of the mesoporous active layer, (iii) corrosion of the metal in contact with the liquid electrolytes used in DSSCs, (iv) reduced absorption in the active layer due to excessive metal particle density, and (v) losses at the metal/sensitizer/TiO$_2$ interface due to inefficient charge injection into the semiconductor, which would decrease device FF and V_{oc}.

To mediate these detrimental effects, metal nanostructures are typically coated with a passivation layer of either SiO$_2$[42,45,110,111] or TiO$_2$.[71,131,136,176–183] The electronic effects of the composition and thickness of the passivation layer have been discussed in Section 3.3.3. Thicker dielectric layers (>5 nm) are often preferred as it is easier to synthesize uniform coatings covering the entire metal surface; thicker layers also afford better thermal and chemical stability, and electronic isolation of the nanostructures from the surrounding sensitizer. However, at layer thicknesses >10 nm, plasmon resonance broadening and damping can severely reduce light trapping capabilities. Further, since the electromagnetic fields decay rapidly from the metal surface, the thickness of the capping layer should be controlled to minimize reduction in both radiative enhancement by near-field coupling as well as non-radiative enhancement *via* PRET.

On the contrary, thinner passivation layers of ≤3 nm are strongly desired to not only enable strong coupling with the sensitizer but also allow hot carrier transfer over the oxide tunneling barrier.[106] However, achieving controllable, uniform thin oxide layers without aggregating the nanostructures remains a challenge. In addition, hot electron transfer across the Schottky barrier of the semiconductor suffers from internal losses due to heating; the efficiency of this process, however, may be increased by tailoring the semiconductor/metal interface to lower the Schottky barrier. This can be achieved by either introducing another semi-conducting layer between the metal nanostructure and TiO$_2$,[100] or by introducing molecular bridges[184–187] that are known to enhance electrical conductivity and electron transfer, while minimizing electron recombination at trap states localized on the TiO$_2$ surface.[188,189]

Other challenges in plasmonic enhancement of MSCs include design of metal nanostructures that primarily scatter light with minimal intrinsic absorption losses.[190] Since large nanoparticles can be detrimental to charge transport in the solar cell, absorption losses may be minimized by either designing nanostructures with complex morphologies and tunable scattering cross-sections, or by selecting a nanostructure composition with low imaginary component of the dielectric constant. As discussed in Section 3.3, Al is being considered a strong contender to supplement the traditional Au or Ag, although tuning Al resonance beyond the UV remains a challenge. Semiconductor and transparent conducting oxide (TCO) nanostructures that support surface plasmons are also promising candidates for enhancing light trapping in MSCs as discussed in the next section. Finally, optimization of the nanostructure particle densities in MSCs is often challenging but necessary to minimize phonon generation and maintain sufficient absorber volume at high particle densities.[30,131]

7. The promise of new plasmonic materials beyond noble metals

Beyond the traditional noble metals of Au, Ag, and Cu, recent findings of LSPRs in semiconductor nanocrystals have opened up a new regime in plasmonics, allowing light capture into the far-infrared.[191–193] In fact, LSPRs are no longer being viewed solely as attributes of metal nanoparticles, but rather optical characteristics of a collection of free carriers in nanoscale systems. Since the initial discovery by Zhao *et al.*[194] and Luther *et al.*[195] of plasmons in the Cu$_{2-x}$S nanocrystal family, this burgeoning field has made tremendous strides, and metal-like LSPRs have now been found in oxides, nitrides, tellurides, sulfides, and selenides.[196–208] LSPRs in semiconductors are generated in three possible ways: (i) by introducing free carriers extrinsically in the form of dopant atoms, such as those in oxides and nitrides (Al:ZnO, ITO, *etc.*);[201–204,206,207] (ii) by "self-doping" intrinsically where free carriers arise from variable oxidation state of the element in non-stoichiometric phase, such as in copper chalcogenides (Cu$_{2-x}$S, Cu$_{2-x}$Se, Cu$_{2-x}$Te *etc.*)[194–198,200,208] and oxygen-deficient metal oxides (WO$_{3-x}$, MoO$_{3-x}$);[199,201,205]

This journal is © The Royal Society of Chemistry 2016

Energy Environ. Sci., 2016, **9**, 1577–1601 | **1595**

and (iii) by strongly correlated electrons where free carriers arise due to the intrinsic electronic structure of the semiconductor, giving rise to conductive behavior, such as in transition metal dioxides (VO_2, RuO_2).

Plasmons in semiconductor nanocrystals have several unique features. First, noble metals have high carrier densities (10^{23} cm^{-3}) that cannot be appreciably altered; however, carrier concentrations in semiconductors can be varied from 10^{16} to 10^{21} cm^{-3} by controlled doping enabling very high tunability of LSPRs from the near-infrared to THz regime. And second, noble metals have high optical losses due to both interband and intraband transitions. On the contrary, semiconductors qualify as low-loss materials due to their large bandgap, which ensures almost no interband transition losses, and lower imaginary part of the permittivity in the infrared which significantly reduces intraband losses.[191,193,209] These qualifications collectively suggest LSPRs in semiconductor nanocrystals can be manipulated to generate desirable optical properties to enhance light harvesting in MSCs. A recent work by Rosenthal and co-workers demonstrated this effect; the authors compared the performance of degenerately doped plasmonic $Cu_xIn_yS_2$ quantum dots with its non-plasmonic counterpart (no cationic vacancies) in solar cells and observed an 11.5% relative increase in IPCE with the former.[200] However, despite their promise, the full potential of semiconductor LSPRs in solar cells has yet to be realized due to their poor tunability in the visible region and lower carrier densities than traditional metal nanoparticles, resulting in minimal light scattering. These challenges have been addressed with recent efforts in metal–semiconductor hybrids either in core/shell architectures or dimer geometries.[210–213] The unique combination of metal and semiconductor components on a single nanoplatform enables broadband tunability of optical resonances from UV to IR, and provides three degrees of freedom for manipulating LSPRs – shape, size, and modification of carrier density by controlling vacancies. However, these nanostructures have not been employed in solar cells yet to evaluate their device performance and IPCE behavior. While detailed discussion of semiconductor plasmonics and their relevance in MSCs is beyond the scope of this review, readers are encouraged to refer to thorough reviews already published on this topic.[191,192,209,214,215]

8. Other plasmonic photovoltaic systems

While this review article primarily focuses on mesoporous dye-sensitized and perovskite solar cells, plasmonic nanostructures have improved light harvesting in other solar energy conversion systems including photoelectrochemical water splitting,[46] and thin film photovoltaic architectures such as silicon solar cells and organic photovoltaics.[216] Whereas the plasmonic enhancement mechanisms in water splitting are essentially the same as liquid-electrolyte based mesoporous solar cells, in planar photovoltaic architectures plasmonic enhancements are correlated to the minority carrier diffusion lengths. Similar to MSCs,

both light scattering and near-field generation play a crucial role in thin film solar cells. However, the minority carrier diffusion lengths of the plasmonically enhanced excitons must be larger than the thickness of the active layer for the carriers to be collected. Hot electron transfer may also be envisioned in planar PVs specifically if metal nanostructures are placed at the interface of the active layer and charge transport layer. Unlike mesoporous solar cells where plasmonic enhancement is largely achieved by incorporating discrete nanostructures supporting LSPRs, the planar architecture of thin-film PVs allows integration of waveguide structures that support SPP modes resulting in improved optical path length of the devices. The planar geometry is also ideal to integrate plasmonic antireflection coatings to enable coupling of back-scattered light. Unlike traditional dielectric coatings, plasmonic antireflection coatings are highly tunable *via* geometry, composition, and surrounding dielectric medium. Further, these coatings can be designed to improve the angular response of a planar solar cell. An important aspect of incorporating plasmonic components in all classes of solar cells is the enhanced light harvesting enables the design of thinner active layers without sacrificing absorption; this effect is even more prominent in thin film PVs. Therefore plasmon-enhanced PVs are ultimately expected to yield more economical solar cells with smaller footprint. Since this review specifically focuses on mesoporous solar cells, an in depth review of plasmon-enhanced thin film PVs is beyond the scope of this article. However, readers are directed to other excellent reviews that cover these topics.[217–223]

9. Summary and future prospects

This review article provides a comprehensive overview of progress in plasmon-enhanced mesoporous solar cells (MSCs), including perovskite solar cells (PSCs) and dye-sensitized solar cells (DSSCs), in the past decade. We have discussed the mechanisms of radiative and non-radiative plasmonic-enhancement, including light scattering and near-field coupling, as well as hot electron transfer (HET) and plasmon resonant energy transfer (PRET) and their relevance in MSCs. A survey of the literature demonstrates DSSCs primarily benefit from radiative enhancement both in the near-field and far-field, as well as PRET resulting in increased photocurrent. In PSCs, plasmon-enhanced light harvesting gives rise to a modest increase in photocurrent, by both enhancing optical absorption and decreasing exciton binding energy. Recent evidence also shows HET from plasmons to perovskites drives an increase in open circuit voltage, improving overall device performance, but further work is required to confirm this hypothesis. We also discuss the challenges in integration of plasmonic nanostructures in MSCs and surface passivation techniques to surmount these challenges. Further, we provide a brief overview of LSPRs in semiconductor nanocrystals and their promise in MSCs as low-loss, highly-tunable optical materials. Finally, distinct from other reviews, we also summarize the progress in spectroscopic investigation of plasmon-enhanced DSSCs and PSCs with time-resolved spectroscopies

to probe fundamental charge transport and other optically-induced phenomena.

Plasmonic enhancement in solar cells has progressed rapidly in the past decade from thin-film Si photovoltaics (PVs) to perovskite devices. We anticipate in the next decade, new plasmonic materials will be discovered, and new PV architectures will be realized for further advances in efficiency and ultimately in commercial feasibility. Specifically, integrating mixed-halide organic–inorganic and all-inorganic perovskites with plasmonic nanostructures is very promising. The high air- and moisture-stability of $MAPbI_{3-x}Br_x$ perovskite relative to their pure iodide counterpart is highly desirable for commercialization; however, mixed-halides typically have their band-edge in the visible.[10,224–227] By coupling plasmonic nanostructures resonant in the IR with $MAPbI_{3-x}Br_x$, broadband solar light capture can be realized. Further, plasmonic enhancement *via* HET will likely be possible since a direct overlap of LSPR and perovskite absorption is not required. LSPRs may also be engineered into the cathode of PSCs, which is typically Au or Ag, by nanostructuring the electrode with top-down approaches to ultimately enable long-range SPP modes to couple to the optical resonances of the perovskites. Finally, further understanding of charge transport processes at the dye/metal and perovskite/metal interfaces with time-resolved spectroscopies is necessary to probe electronic processes at early time-scales. Single-particle measurements at these interfaces with super-resolution imaging would also be highly relevant to minimize ambiguities in ensemble measurements.

Acknowledgements

References

1 B. E. Hardin, H. J. Snaith and M. D. McGehee, *Nat. Photonics*, 2012, **6**, 162–169.

2 M. Grätzel, *Acc. Chem. Res.*, 2009, **42**, 1788–1798.

3 S. Kazim, M. K. Nazeeruddin, M. Gratzel and S. Ahmad, *Angew. Chem., Int. Ed.*, 2014, **53**, 2812–2824.

4 J. Burschka, N. Pellet, S.-J. Moon, R. Humphry-Baker, P. Gao, M. K. Nazeeruddin and M. Gratzel, *Nature*, 2013, **499**, 316–332.

5 I. Chung, B. Lee, J. He, R. P. H. Chang and M. G. Kanatzidis, *Nature*, 2012, **485**, 486–489.

6 M. Law, L. E. Greene, J. C. Johnson, R. Saykally and P. Yang, *Nat. Mater.*, 2005, **4**, 455–459.

7 S. Mathew, A. Yella, P. Gao, R. Humphry-Baker, B. F. E. Curchod, N. Ashari-Astani, I. Tavernelli, U. Rothlisberger, M. K. Nazeeruddin and M. Grätzel, *Nat. Chem.*, 2014, **6**, 242–247.

8 A. Yella, H. W. Lee, H. N. Tsao, C. Yi, A. K. Chandiran, M. K. Nazeeruddin, E. W. D. Diau, C. Y. Yeh, S. M. Zakeeruddin and M. Grätzel, *Science*, 2011, **334**, 629–634.

9 J.-H. Yum, E. Baranoff, S. Wenger, M. K. Nazeeruddin and M. Grätzel, *Energy Environ. Sci.*, 2011, **4**, 842–857.

10 M. M. Lee, J. Teuscher, T. Miyasaka, T. N. Murakami and H. J. Snaith, *Science*, 2012, **338**, 643–648.

11 J. M. Ball, M. M. Lee, A. Hey and H. J. Snaith, *Energy Environ. Sci.*, 2013, **6**, 1739–1743.

12 W. A. Laban and L. Etgar, *Energy Environ. Sci.*, 2013, **6**, 3249–3253.

13 P. Qin, S. Tanaka, S. Ito, N. Tetreault, K. Manabe, H. Nishino, M. K. Nazeeruddin and M. Gratzel, *Nat. Commun.*, 2014, **5**, 3834.

14 J. H. Heo, S. H. Im, J. H. Noh, T. N. Mandal, C.-S. Lim, J. A. Chang, Y. H. Lee, H.-j. Kim, A. Sarkar, M. K. Nazeeruddin, M. Grätzel and S. I. Seok, *Nat. Photonics*, 2013, **7**, 486–491.

15 M. Liu, M. B. Johnston and H. J. Snaith, *Nature*, 2013, **501**, 395–399.

16 H. J. Snaith, *J. Phys. Chem. Lett.*, 2013, **4**, 3623–3630.

17 J. B. Baxter, *J. Vac. Sci. Technol., A*, 2012, **30**, 020801.

18 M. A. Green and S. Pillai, *Nat. Photonics*, 2012, **6**, 130–132.

19 A. Polman and H. A. Atwater, *Nat. Mater.*, 2012, **11**, 174–177.

20 H. A. Atwater and A. Polman, *Nat. Mater.*, 2010, **9**, 205–213.

21 G. W. P. Adhyaksa, S.-W. Baek, G. I. Lee, D. K. Lee, J.-Y. Lee and J. K. Kang, *ChemSusChem*, 2014, **7**, 2461–2468.

22 M. D. Brown, T. Suteewong, R. S. S. Kumar, V. D. Innocenzo, A. Petrozza, M. M. Lee, U. Wiesner and H. J. Snaith, *Nano Lett.*, 2011, **11**, 438–445.

23 P.-Y. Chen, X. Dang, M. T. Klug, J. Qi, D. Courchesne, F. J. Burpo, N. Fang, P. T. Hammond and A. M. Belcher, *ACS Nano*, 2013, 6563–6574.

24 B. Ding, B. J. Lee, M. Yang, H. S. Jung and J. K. Lee, *Adv. Energy Mater.*, 2011, **1**, 415–421.

25 H. Dong, Z. Wu, A. El-Shafei, B. Xia, J. Xi, S. Ning, B. Jiao and X. Hou, *J. Mater. Chem. A*, 2015, **3**, 4659–4668.

26 J. Du, J. Qi, D. Wang and Z. Tang, *Energy Environ. Sci.*, 2012, **5**, 6914–6918.

27 Y. H. Jang, Y. J. Jang, S. T. Kochuveedu, M. Byun, Z. Lin and D. H. Kim, *Nanoscale*, 2014, **6**, 1823–1832.

28 S. Wooh, Y.-G. Lee, M. N. Tahir, D. Song, M. Meister, F. Laquai, W. Tremel, J. Bisquert, Y. S. Kang and K. Char, *J. Mater. Chem. A*, 2013, **1**, 12627–12634.

29 J. Yun, S. H. Hwang and J. Jang, *ACS Appl. Mater. Interfaces*, 2015, **7**, 2055–2063.

30 H. F. Zarick, W. R. Erwin, A. Boulesbaa, O. Hurd, J. A. Webb, A. Puretzky, D. Geohegan and R. Bardhan, *ACS Photonics*, 2016, DOI: 10.1021/acsphotonics.5b00552.

31 C. F. Bohren and D. R. Huffman, *Absorption and Scattering of Light by Small Particles*, Wiley, 1983.

32 S. A. Maier, *Plasmonics: Fundamentals and Applications*, Springer, 2007.

33 H. C. van de Hulst, *Light Scattering by Small Particles*, Dover Publications, Inc., New York, N.Y., 1981.

34 L. Novotny and N. v. Hulst, *Nat. Photonics*, 2011, **5**, 83–90.

This journal is © The Royal Society of Chemistry 2016

Energy Environ. Sci., 2016, **9**, 1577–1601 | **1597**

35 K. L. Kelly, E. Coronado, L. L. Zhao and G. C. Schatz, *J. Phys. Chem. B*, 2003, **107**, 668–677.

36 V. Myroshnychenko, J. Rodriguez-Fernandez, I. Pastoriza-Santos, A. M. Funston, C. Novo, P. Mulvaney, L. M. Liz-Marzan and F. J. G. d. Abajo, *Chem. Soc. Rev.*, 2008, **37**, 1792–1805.

37 P. K. Jain, K. S. Lee, I. H. El-Sayed and M. A. El-Sayed, *J. Phys. Chem. B*, 2006, **110**, 7238–7248.

38 J. M. Pitarke, V. M. Silkin, E. V. Chulkov and P. M. Echenique, *J. Opt. A: Pure Appl. Opt.*, 2005, **7**, S73–S84.

39 M. Rycenga, C. M. Cobley, J. Zeng, W. Li, C. H. Moran, Q. Zhang, D. Qin and Y. Xia, *Chem. Rev.*, 2011, **111**, 3669–3712.

40 S. Linic, P. Christopher and D. B. Ingram, *Nat. Mater.*, 2011, **10**, 911–921.

41 H. F. Zarick, W. R. Erwin, J. Aufrecht, A. Coppola, B. R. Rogers, C. L. Pint and R. Bardhan, *J. Mater. Chem. A*, 2014, **2**, 7088–7098.

42 J. A. Webb, W. R. Erwin, H. F. Zarick, J. Aufrecht, H. W. Manning, M. J. Lang, C. L. Pint and R. Bardhan, *J. Phys. Chem. C*, 2014, **118**, 3696–3707.

43 R. Carminati, J. J. Greffet, C. Henkel and J. M. Vigoureux, *Opt. Commun.*, 2006, **261**, 368–375.

44 P. K. Jain, W. Huang and M. A. El-Sayed, *Nano Lett.*, 2007, **7**, 2080–2088.

45 J. R. Lakowicz, *Anal. Biochem.*, 2005, **337**, 171–194.

46 S. C. Warren and E. Thimsen, *Energy Environ. Sci.*, 2012, **5**, 5133.

47 A. V. Zayats, I. I. Smolyaninov and A. A. Maradudin, *Phys. Rep.*, 2005, **408**, 131–314.

48 W.-S. Chang, B. a. Willingham, L. S. Slaughter, B. P. Khanal, L. Vigderman, E. R. Zubarev and S. Link, *Proc. Natl. Acad. Sci. U. S. A.*, 2011, **108**, 19879–19884.

49 J. A. Fan, C. Wu, K. Bao, J. Bao, R. Bardhan, N. J. Halas, V. N. Manoharan, P. Nordlander, G. Shvets and F. Capasso, *Science*, 2010, **328**, 1135–1138.

50 A. Tao, P. Sinsermsuksakul and P. Yang, *Nat. Nanotechnol.*, 2007, **2**, 435–440.

51 M. K. Gangishetty, R. W. J. Scott and T. L. Kelly, *Langmuir*, 2014, **30**, 14352–14359.

52 H.-L. Hsu, T.-Y. Juang, C.-P. Chen, C.-M. Hsieh, C.-C. Yang, C.-L. Huang and R.-J. Jeng, *Sol. Energy Mater. Sol. Cells*, 2015, **140**, 224–231.

53 *The Mie Theory: Basics and Applications*, ed. W. Hergert and T. Wriedt, Springer, New York, NY, 2012.

54 W. T. Doyle, *Phys. Rev. B: Condens. Matter Mater. Phys.*, 1989, **39**, 9852–9858.

55 X. Fan, W. Zheng and D. J. Singh, *Light: Sci. Appl.*, 2014, **3**, e179.

56 Q. Fu and W. Sun, *Appl. Opt.*, 2001, **40**, 1354–1361.

57 C. Sönnichsen, T. Franzl, T. Wilk, G. v. Plessen and J. Feldmann, *New J. Phys.*, 2002, **4**, 93.

58 K.-S. Lee and M. A. El-Sayed, *J. Phys. Chem. B*, 2006, **110**, 19220–19225.

59 E. Hao, G. C. Schatz and J. T. Hupp, *J. Fluoresc.*, 2004, **14**, 331–341.

60 I. O. Sosa, C. Noguez and R. G. Barrera, *J. Phys. Chem. B*, 2003, **107**, 6269–6275.

61 R. Bardhan, S. Mukherjee, N. Mirin, S. D. Levit, P. Nordlander and N. J. Halas, *J. Phys. Chem. C*, 2010, **114**, 7378–7383.

62 N. K. Grady, N. J. Halas and P. Nordlander, *Chem. Phys. Lett.*, 2004, **399**, 167–171.

63 P. B. Johnson and R. W. Christy, *Phys. Rev. B: Solid State*, 1972, **6**, 4370–4379.

64 A. Pinchuk, G. V. Plessen and U. Kreibig, *J. Phys. D: Appl. Phys.*, 2004, **37**, 3133–3139.

65 J. M. Pitarke, V. M. Silkin, E. V. Chulkov and P. M. Echenique, *Rep. Prog. Phys.*, 2007, **70**, 1–87.

66 H. Dong, Z. Wu, F. Lu, Y. Gao, A. El-Shafei, B. Jiao, S. Ning and X. Hou, *Nano Energy*, 2014, **10**, 181–191.

67 S. H. Hwang, D. H. Shin, J. Yun, C. Kim, M. Choi and J. Jang, *Chemistry*, 2014, **20**, 4439–4446.

68 W. Jiang, H. Liu, L. Yin and Y. Ding, *J. Mater. Chem. A*, 2013, **1**, 6433–6440.

69 H. Y. Kim, W. Y. Rho, H. Y. Lee, Y. S. Park and J. S. Suh, *Sol. Energy*, 2014, **109**, 61–69.

70 B. Lim, H. Yun, S. Kwon, Y. Kim and D. S. Chung, *RSC Adv.*, 2014, **4**, 48236–48244.

71 S. J. Lin, K. C. Lee, J. L. Wu and J. Y. Wu, *Appl. Phys. Lett.*, 2011, **99**, 043306.

72 S. J. Lin, K. C. Lee, J. L. Wu and J. Y. Wu, *Sol. Energy*, 2012, **86**, 2600–2605.

73 K.-S. Lee and M. A. El-Sayed, *J. Phys. Chem. B*, 2005, **109**, 20331–20338.

74 A. Liebsch and B. N. J. Persson, *J. Phys. C: Solid State Phys.*, 1983, **16**, 5375–5391.

75 S. Link, M. B. Mohamed and M. A. El-Sayed, *J. Phys. Chem. B*, 1999, **103**, 3073–3077.

76 F. Wang and Y. R. Shen, *Phys. Rev. Lett.*, 2006, **97**, 206806.

77 T. R. Jensen, M. L. Duval, K. L. Kelly, A. A. Lazarides, G. C. Schatz and R. P. Van Duyne, *J. Phys. Chem. B*, 1999, **103**, 9846–9853.

78 H. F. Zarick, O. Hurd, J. A. Webb, C. Hungerford, W. R. Erwin and R. Bardhan, *ACS Photonics*, 2014, **1**, 806–811.

79 J. A. Schuller, E. S. Barnard, W. Cai, Y. C. Jun, J. S. White and M. l. Brongersma, *Nat. Mater.*, 2010, **9**, 193–204.

80 M. Haggui, M. Dridi, J. Plain, S. Marguet, H. Perez, G. C. Schatz, G. P. Wiederrecht, S. K. Gray and R. Bachelot, *ACS Nano*, 2012, **6**, 1299–1307.

81 M. Rycenga, X. Xia, C. H. Moran, F. Zhou, D. Qin, Z. Y. Li and Y. Xia, *Angew. Chem., Int. Ed.*, 2011, **50**, 5473–5477.

82 M. Rycenga, M. H. Kim, P. H. Camargo, C. Cobley, Z. Y. Li and Y. Xia, *J. Phys. Chem. A*, 2009, **113**, 3932–3939.

83 M. B. Mohamed, V. Volkov, S. Link and M. a. El-Sayed, *Chem. Phys. Lett.*, 2000, **317**, 517–523.

84 J. Gersten and A. Nitzan, *J. Chem. Phys.*, 1980, **73**, 3023–3037.

85 P. F. Liao and A. Wokaun, *J. Chem. Phys.*, 1982, **76**, 751–752.

86 M. W. Knight, H. Sobhani, P. Nordlander and N. J. Halas, *Science*, 2011, **332**, 702–704.

87 J. Li, S. K. Cushing, F. Meng, T. R. Senty, A. D. Bristow and N. Wu, *Nat. Photonics*, 2015, **9**, 601–607.

88 C. Clavero, *Nat. Photonics*, 2014, **8**, 95–103.

89 X. Li, D. Xiao and Z. Zhang, *New J. Phys.*, 2013, **15**, 023011.

1598 | *Energy Environ. Sci.*, 2016, **9**, 1577–1601

This journal is © The Royal Society of Chemistry 2016

90 R. Bingham, J. Mendonça and J. Dawson, *Phys. Rev. Lett.*, 1997, **78**, 247–249.

91 Y. Gao, Z. Yuan and S. Gao, *J. Chem. Phys.*, 2011, **134**, 1–5.

92 M. L. Brongersma, N. J. Halas and P. Nordlander, *Nat. Nanotechnol.*, 2015, **10**, 25–34.

93 A. Manjavacas, J. G. Liu, V. Kulkarni and P. Nordlander, *ACS Nano*, 2014, 7630–7638.

94 R. Bardhan, W. Chen, M. Bartels, C. Perez-Torres, M. F. Botero, R. W. McAninch, A. Contreras, R. Schiff, R. G. Pautler, N. J. Halas and A. Joshi, *Nano Lett.*, 2010, **10**, 4920–4928.

95 R. Bardhan, W. Chen, C. Perez-Torres, M. Bartels, R. M. Huschka, L. Zhao, E. Morosan, R. Pautler, A. Joshi and N. J. Halas, *Adv. Funct. Mater.*, 2009, **19**, 3901–3909.

96 R. Bardhan, S. Lal, A. Joshi and N. J. Halas, *Acc. Chem. Res.*, 2011, **44**, 936–946.

97 W. Chen, C. Ayala-Orozco, N. C. Biswal, C. Perez-Torres, M. Bartels, R. Bardhan, G. Stinnet, X.-D. Liu, B. Ji, A. Deorukhkar, L. V. Brown, S. Guha, R. G. Pautler, S. Krishnan, N. J. Halas and A. Joshi, *Nanomedicine*, 2014, **9**, 1209–1222.

98 M.-R. Choi, R. Bardhan, K. J. Stanton-Maxey, H. N. S. Badve, K. M. Stantz, N. Cao, N. J. Halas and S. E. Clare, *Cancer Nanotechnol.*, 2012, **3**, 47–54.

99 J. A. Webb and R. Bardhan, *Nanoscale*, 2014, **6**, 2502–2530.

100 K. Wu, J. Chen, J. R. McBride and T. Lian, *Science*, 2015, **349**, 3584–3588.

101 M. W. Knight, Y. Wang, A. S. Urban, A. Sobhani, B. Y. Zheng, P. Nordlander and N. J. Halas, *Nano Lett.*, 2013, **13**, 1687–1692.

102 S. Mubeen, J. Lee, W.-R. Lee, N. Singh, G. D. Stucky and M. Moskovits, *ACS Nano*, 2014, **8**, 6066–6073.

103 S. Mubeen, J. Lee, N. Singh, S. Krämer, G. D. Stucky and M. Moskovits, *Nat. Nanotechnol.*, 2013, **8**, 247–251.

104 S. Mukherjee, L. Zhou, A. M. Goodman, N. Large, C. Ayala-Orozco, Y. Zhang, P. Nordlander and N. J. Halas, *J. Am. Chem. Soc.*, 2014, **136**, 64–67.

105 A. Sobhani, M. W. Knight, Y. Wang, B. Zheng, N. S. King, L. V. Brown, Z. Fang, P. Nordlander and N. J. Halas, *Nat. Commun.*, 2013, **4**, 1643.

106 W. R. Erwin, A. Coppola, H. F. Zarick, P. Arora, K. J. Miller and R. Bardhan, *Nanoscale*, 2014, **6**, 12626–12634.

107 A. O. Govorov, H. Zhang and Y. K. Gun'Ko, *J. Phys. Chem. C*, 2013, **117**, 16616–16631.

108 S. Mukherjee, H. Sobhani, J. B. Lassiter, R. Bardhan, P. Nordlander and N. J. Halas, *Nano Lett.*, 2010, **10**, 2694–2701.

109 Z. Fang, J. Cai, Z. Yan, P. Nordlander, N. J. Halas and X. Zhu, *Nano Lett.*, 2011, **11**, 4475–4479.

110 F. Hao, P. Nordlander, Y. Sonnefraud, P. Van Dorpe and S. a. Maier, *ACS Nano*, 2009, **3**, 643–652.

111 F. Hao, Y. Sonnefraud, P. Van Dorpe, S. A. Maier, N. J. Halas and P. Nordlander, *Nano Lett.*, 2008, **8**, 3983–3988.

112 J. A. Fan, K. Bao, C. Wu, J. Bao, R. Bardhan, N. J. Halas, V. N. Manoharan, G. Shvets, P. Nordlander and F. Capasso, *Nano Lett.*, 2010, **10**, 4680–4685.

113 J. B. Lassiter, H. Sobhani, J. A. Fan, J. Kundu, F. Capasso, P. Nordlander and N. J. Halas, *Nano Lett.*, 2010, **10**, 3184–3189.

114 M. Hentschel, D. Dregely, R. Vogelgesang, H. Giessen and N. Liu, *ACS Nano*, 2011, **5**, 2042–2050.

115 S. K. Cushing, J. Li, J. Bright, B. T. Yost, P. Zheng, A. D. Bristow and N. Wu, *J. Phys. Chem. C*, 2015, **119**, 16239–16244.

116 S. K. Cushing, J. Li, F. Meng, T. R. Senty, S. Suri, M. Zhi, M. Li, A. D. Bristow and N. Wu, *J. Am. Chem. Soc.*, 2012, **134**, 15033–15041.

117 A. Pinchuk and U. Kreibig, *New J. Phys.*, 2003, **5**, 151.151.

118 H. Choi, W. T. Chen and P. Kamat, *ACS Nano*, 2012, **6**, 4418–4427.

119 Q. Wang, T. Butburee, X. Wu, H. J. Chen, G. Liu and L. Z. Wang, *J. Mater. Chem. A*, 2013, **1**, 13524–13531.

120 A. Anderson, K. S. Deryckx, X. G. Xu, G. Steinmeyer and M. B. Raschke, *Nano Lett.*, 2010, **10**, 2519–2524.

121 Y. Nishiyama, K. Imaeda, K. Imura and H. Okamoto, *J. Phys. Chem. C*, 2015, **119**, 16125–16222.

122 C. Sönnichsen, T. Franzl, T. Wilk, G. von Plessen, J. Feldmann, O. Wilson and P. Mulvaney, *Phys. Rev. Lett.*, 2002, **88**, 077402.

123 C. Wen, K. Ishikawa, M. Kishima and K. Yamada, *Sol. Energy Mater. Sol. Cells*, 2000, **61**, 339–351.

124 C. Noguez, *J. Phys. Chem. C*, 2007, **111**, 3806–3819.

125 C. H. Lin and C. W. Liu, *Sensors*, 2013, **10**, 8797–8826.

126 Y. H. Su, Y. F. Ke, S. L. Cai and Q. Y. Yao, *Light: Sci. Appl.*, 2012, **1**, e14(15).

127 D. Zheng, X. Pang, M. Wang, Y. He, C. Lin and Z. Lin, *Chem. Mater.*, 2015, **27**, 5271–5278.

128 A. Dabirian and N. Taghavinia, *ACS Appl. Mater. Interfaces*, 2015, **7**, 14926–14932.

129 C. Nahm, H. Choi, J. Kim, D. R. Jung, C. Kim, J. Moon, B. Lee and B. Park, *Appl. Phys. Lett.*, 2011, **99**, 253107.

130 Q. Xu, F. Liu, Y. Liu, K. Cui, X. Feng, W. Zhang and Y. Huang, *Sci. Rep.*, 2013, **3**, 2112.

131 N. Chander, A. F. Khan, E. Thouti and S. K. Sardana, *Sol. Energy*, 2014, **109**, 11–23.

132 S. Chang, Q. Li, X. Xiao, K. Y. Wong and T. Chen, *Energy Environ. Sci.*, 2012, **5**, 9444–9448.

133 X. Dang, J. Qi, M. T. Klug, P.-Y. Chen, D. S. Yun, N. X. Fang, P. T. Hammond and A. M. Belcher, *Nano Lett.*, 2013, **13**, 637–642.

134 S. W. Sheehan, H. Noh, G. W. Brudvig, H. Cao and C. A. Schmuttenmaer, *J. Phys. Chem. C*, 2013, **117**, 927–934.

135 M. K. Gangishetty, K. E. Lee, R. W. J. Scott and T. L. Kelly, *ACS Appl. Mater. Interfaces*, 2013, **5**, 11044–11051.

136 W.-L. Liu, F.-C. Lin, Y.-C. Yang, C.-H. Huang, S. Gwo, M. H. Huang and J.-S. Huang, *Nanoscale*, 2013, **5**, 7953–7962.

137 K. A. Willets and R. P. Van Duyne, *Annu. Rev. Phys. Chem.*, 2007, **58**, 267–297.

138 B. Lim and Y. Xia, *Angew. Chem., Int. Ed.*, 2011, **50**, 76–85.

139 C. Burda, X. Chen, R. Narayanan and M. A. El-Sayed, *Chem. Rev.*, 2005, **105**, 1025–1102.

140 R. Narayanan, M. Deepa, A. K. Srivastava and S. M. Shivaprasad, *ChemPhysChem*, 2014, **15**, 1106–1115.

This journal is © The Royal Society of Chemistry 2016

Energy Environ. Sci., 2016, **9**, 1577–1601 | **1599**

141 S. P. Ng, X. Lu, N. Ding, C. M. L. Wu and C. S. Lee, *Sol. Energy*, 2014, **99**, 115–125.

142 N. C. Jeong, C. Prasittichai and J. T. Hupp, *Langmuir*, 2011, **27**, 14609–14614.

143 J. Qi, X. Dang, P. T. Hammond and A. M. Belcher, *ACS Nano*, 2011, **5**, 7108–7116.

144 G. V. Naik, J. L. Schroeder, X. Ni, A. V. Kildishev, T. D. Sands and A. Boltasseva, *Opt. Mater. Express*, 2012, **2**, 478–489.

145 G. V. Naik, V. M. Shalaev and A. Boltasseva, *Adv. Mater.*, 2013, **25**, 3264–3294.

146 B. Wiley, Y. Sun, B. Mayers and Y. Xia, *Chemistry*, 2005, **11**, 454–463.

147 M. W. Knight, N. S. King, L. Liu, H. O. Everitt, P. Nordlander and N. J. Halas, *ACS Nano*, 2014, **8**, 834–840.

148 M. W. Knight, L. Liu, Y. Wang, L. Brown, S. Mukherjee, N. S. King, H. O. Everitt, P. Nordlander and N. J. Halas, *Nano Lett.*, 2012, **12**, 6000–6004.

149 Y. A. Akimov and W. S. Koh, *Plasmonics*, 2011, **6**, 155–161.

150 N. P. Hylton, X. F. Li, V. Giannini, K. H. Lee, N. J. Ekins-Daukes, J. Loo, D. Vercruysse, P. Van Dorpe, H. Sodabanlu, M. Sugiyama and S. A. Maier, *Sci. Rep.*, 2013, **3**, 2874.

151 Q. Xu, F. Liu, Y. Liu, W. Meng, K. Cui, X. Feng, W. Zhang and Y. Huang, *Opt. Express*, 2014, **22**, A301.

152 V. Kochergin, L. Neely, C.-Y. Jao and H. D. Robinson, *Appl. Phys. Lett.*, 2011, **98**, 133305.

153 H.-Y. Kim, D. H. Song, H. Yoon and J. S. Suh, *RSC Adv.*, 2015, **5**, 27464–27469.

154 M. Karg, T. A. F. König, M. Retsch, C. Stelling, P. M. Reichstein, T. Honold, M. Thelakkat and A. Fery, *Mater. Today*, 2015, **18**, 185–205.

155 R. A. Naphade, M. Tathavadekar, J. P. Jog, S. Agarkar and S. Ogale, *J. Mater. Chem. A*, 2014, **2**, 975–984.

156 H. Ninsonti, W. Chomkitichai, A. Baba, N. Wetchakun, W. Kangwansupamonkon, S. Phanichphant, K. Shinbo, K. Kato and F. Kaneko, *Hindawi*, 2014, 1–8.

157 I. K. Ding, J. Zhu, W. Cai, S.-J. Moon, N. Cai, P. Wang, S. M. Zakeeruddin, M. Grätzel, M. L. Brongersma, Y. Cui and M. D. McGehee, *Adv. Energy Mater.*, 2011, **1**, 52–57.

158 C. Hägglund, M. Zäch and B. Kasemo, *Appl. Phys. Lett.*, 2008, **92**, 013113.

159 Y. Nishijima, K. Ueno, Y. Yokota, K. Murakoshi and H. Misawa, *J. Phys. Chem. Lett.*, 2010, **1**, 2031–2036.

160 N. Yang, Q. Yuan, J. Zhai, T. Wei, D. Wang and L. Jiang, *ChemSusChem*, 2012, **5**, 572–576.

161 W. L. Barnes, *J. Opt. A: Pure Appl. Opt.*, 2006, **8**, S87–S93.

162 W. Zhang, M. Saliba, S. D. Stranks, Y. Sun, X. Shi, U. Wiesner and H. J. Snaith, *Nano Lett.*, 2013, **13**, 4505–4510.

163 S. H. Chang, K. F. Lin, C. H. Chiang, S. H. Chen and C. G. Wu, *Sci. World J.*, 2014, **2014**, 1–6.

164 M. Saliba, W. Zhang, V. M. Burlakov, S. D. Stranks, Y. Sun, J. M. Ball, M. B. Johnston, A. Goriely, U. Wiesner and H. J. Snaith, *Adv. Funct. Mater.*, 2015, **25**, 5038–5046.

165 Z. Yuan, Z. Wu, S. Bai, Z. Xia, W. Xu, T. Song, H. Wu, L. Xu, J. Si, Y. Jin and B. Sun, *Adv. Energy Mater.*, 2015, **5**, 150038.

166 M. Qian, M. Li, X.-B. Shi, H. Ma, Z.-K. Wang and L.-S. Liao, *J. Mater. Chem. A*, 2015, **3**, 13533–13539.

167 K. Yan, M. Long, Z. Chen, T. Zhang, Y. Xiao, X. Zeng, J. Chen and J. Xu, *Nanoscale*, 2015, 1–9.

168 S. Carretero-Palacios, M. E. Calvo and H. Miguez, *J. Phys. Chem. C*, 2015, **119**, 18635–18640.

169 P. Zhao, J. Xu, C. Ma, W. Ren, L. Wang, L. Bian and A. Chang, *Scr. Mater.*, 2015, **102**, 51–54.

170 W. Niu, L. A. Ibbotson, D. Leipold, E. Runge, G. V. Prakash and J. J. Baumberg, *Phys. Rev. B: Condens. Matter Mater. Phys.*, 2015, **91**, 161303.

171 J. Even, L. Pedesseau and C. Katan, *ChemPhysChem*, 2014, **15**, 3733–3741.

172 G. V. Hartland, *Chem. Rev.*, 2011, **111**, 3858–3887.

173 E. C. Cho, C. Kim, F. Zhou, C. M. Cobley, K. H. Song, J. Chen, Z.-Y. Li, L. V. Wang and Y. Xia, *J. Phys. Chem. C*, 2009, **113**, 9023–9028.

174 H.-Y. Hsu, C.-W. Cheng, W.-K. Huang, Y.-P. Lee and E. W.-G. Diau, *J. Phys. Chem. C*, 2014, **118**, 16904–16911.

175 F. Kong, S. Dai and K. Wang, *Plasma Sci. Technol.*, 2006, **8**, 531–534.

176 A. Kogo, Y. Takahashi, N. Sakai and T. Tatsuma, *Nanoscale*, 2013, **5**, 7855–7860.

177 S. Muduli, O. Game, V. Dhas, K. Vijayamohanan, K. A. Bogle, N. Valanoor and S. B. Ogale, *Sol. Energy*, 2012, **86**, 1428–1434.

178 B. Sebo, N. Huang, Y. Liu, Q. Tai, L. Liang, H. Hu, S. Xu and X. Z. Zhao, *Electrochim. Acta*, 2013, **112**, 458–464.

179 S. D. Standridge, G. C. Schatz and J. T. Hupp, *J. Am. Chem. Soc.*, 2009, **131**, 8407–8409.

180 X. Zhang, J. Liu, S. Li, X. Tan, M. Yu and J. Du, *RSC Adv.*, 2013, **3**, 18587.

181 W. Hou, P. Pavaskar, Z. Liu, J. Theiss, M. Aykol and S. B. Cronin, *Energy Environ. Sci.*, 2011, **4**, 4650.

182 H. Jung, B. Koo, J. Y. Kim, T. Kim, H. J. Son, B. Kim, J. Y. Kim, D. K. Lee, H. Kim, J. Cho and M. J. Ko, *ACS Appl. Mater. Interfaces*, 2014, **6**, 19191–19200.

183 B. Törngren, K. Akitsu, A. Ylinen, S. Sandén, H. Jiang, J. Ruokolainen, M. Komatsu, T. Hamamura, J. Nakazaki, T. Kubo, H. Segawa, R. Österbacka and J. H. Smått, *J. Colloid Interface Sci.*, 2014, **427**, 54–61.

184 N. J. Tao, *Nat. Nanotechnol.*, 2006, **1**, 173–181.

185 O. Adak, R. Korytár, A. Y. Joe, F. Evers and L. Venkataraman, *Nano Lett.*, 2015, **15**, 3716–3722.

186 C. Nacci, F. Ample, D. Bleger, S. Hecht, C. Joachim and L. Grill, *Nat. Commun.*, 2015, **6**, 7397.

187 A. Nitzan, *J. Phys. Chem. A*, 2001, **105**, 2677–2679.

188 C. Richter and C. A. Schmuttenmaer, *Nat. Nanotechnol.*, 2010, **5**, 769–772.

189 Y. Wang, D. Wu, L. M. Fu, X. C. Ai, D. Xu and J. P. Zhang, *ChemPhysChem*, 2015, **16**, 2253–2259.

190 L. Yuan, F. Chen, C. Zheng, J. Liu and N. Alemu, *Phys. Status Solidi*, 2012, **209**, 1376–1379.

191 A. Comin and L. Manna, *Chem. Soc. Rev.*, 2014, **43**, 3957–3975.

192 J. A. Faucheaux, A. L. D. Stanton and P. K. Jain, *J. Phys. Chem. Lett.*, 2014, **5**, 976–985.

193 R. J. Mendelsberg, G. Garcia, H. Li, L. Manna and D. J. Milliron, *J. Phys. Chem. C*, 2012, **116**, 12226–12231.

194 Y. Zhao, H. Pan, Y. Lou, X. Qiu, J. Zhu and C. Burda, *J. Am. Chem. Soc.*, 2009, **131**, 4253–4261.

195 J. M. Luther, P. K. Jain, T. Ewers and A. P. Alivisatos, *Nat. Mater.*, 2011, **10**, 361–366.

196 T. Wei, Y. Liu, W. Dong, Y. Zhang, C. Huang, Y. Sun, X. Chen and N. Dai, *ACS Appl. Mater. Interfaces*, 2013, **5**, 10473–10477.

197 S.-W. Hsu, W. Bryks and A. R. Tao, *Chem. Mater.*, 2012, **24**, 3765–3771.

198 J. S. Niezgoda, M. A. Harrison, J. R. McBride and S. J. Rosenthal, *Chem. Mater.*, 2012, **24**, 3294–3298.

199 K. Manthiram and A. P. Alivisatos, *J. Am. Chem. Soc.*, 2012, **134**, 3995–3998.

200 J. S. Niezgoda, E. Yap, J. D. Keene, J. R. McBride and S. J. Rosenthal, *Nano Lett.*, 2014, **14**, 3262–3269.

201 G. V. Naik, J. Kim and A. Boltasseva, *Opt. Mater. Express*, 2011, **1**, 1090–1099.

202 P. K. B. Palomaki, E. M. Miller and N. R. Neale, *J. Am. Chem. Soc.*, 2013, **135**, 14142–14150.

203 S. Ghosh, M. Saha, V. D. Ashok, B. Dalal and S. K. De, *J. Phys. Chem. C*, 2015, **119**, 1180–1187.

204 P. Patsalas, N. Kalfagiannis and S. Kassavetis, *Materials*, 2015, **8**, 3128–3154.

205 Z. Lou, Q. Gu, L. Xu, Y. Liao and C. Xue, *Chem. – Asian J.*, 2015, **10**, 1291–1294.

206 T. R. Gordon, T. Paik, D. R. Klein, G. V. Naik, H. Caglayan, A. Boltasseva and C. B. Murray, *Nano Lett.*, 2013, **13**, 2857–2863.

207 A. Calzolari, A. Ruini and A. Catellani, *ACS Photonics*, 2014, **1**, 703–709.

208 I. Kriegel, J. Rodrıguez-Fernandez, A. Wisnet, H. Zhang, C. Waurisch, A. Eychmuller, A. Dubavik, A. O. Govorov and J. Feldmann, *ACS Nano*, 2013, **7**, 4367–4377.

209 P. R. West, S. Ishii, G. V. Naik, N. K. Emani, V. M. Shalaev and A. Boltasseva, *Laser Photonics Rev.*, 2010, **4**, 795–808.

210 X. Liu, C. Lee, W.-C. Law, D. Zhu, M. Liu, M. Jeon, J. Kim, P. N. Prasad, C. Kim and M. T. Swihart, *Nano Lett.*, 2013, **13**, 4333–4339.

211 X. Ye, D. R. Hickey, J. Fei, B. T. Diro, T. Paik, J. Chen and C. B. Murray, *J. Am. Chem. Soc.*, 2014, **136**, 5106–5115.

212 T. R. Gordon and R. E. Schaak, *Chem. Mater.*, 2014, **26**, 5900–5904.

213 M. A. H. Muhammed, M. Döblinger and A. J. Rodríguez-Fernández, *J. Am. Chem. Soc.*, 2015, **137**, 11666–11677.

214 X. Liu and M. T. Swihart, *Chem. Soc. Rev.*, 2014, **43**, 3908–3920.

215 Y. Zhaoab and C. Burda, *Energy Environ. Sci.*, 2012, **5**, 5564–5576.

216 H. R. Stuart and D. G. Hall, *Appl. Phys. Lett.*, 1996, **69**, 2327.

217 K. R. Catchpole and A. Polman, *Opt. Express*, 2008, **16**, 21793–21800.

218 C.-H. Chou and F.-C. Chen, *Nanoscale*, 2014, **6**, 8444–8458.

219 C. Fang, H. Jia, S. Chang, Q. Ruan, P. Wang, T. Chen and J. Wang, *Energy Environ. Sci.*, 2014, **7**, 3431–3438.

220 V. E. Ferry, J. N. Munday and H. A. Atwater, *Adv. Mater.*, 2010, **22**, 4794–4808.

221 Q. Gan, F. J. Bartoli and Z. H. Kafafi, *Adv. Mater.*, 2013, **25**, 2385–2396.

222 M. Gu, Z. Ouyang, B. Jia, N. Stokes, X. Chen, N. Fahim, X. Li, M. J. Ventura and Z. Shi, *Nanophotonics*, 2012, **1**, 235–248.

223 P. Spinelli, V. E. Ferry, J. van de Groep, M. van Lare, M. A. Verschuuren, R. E. I. Schropp, H. A. Atwater and A. Polman, *J. Opt.*, 2012, **14**, 024002.

224 J. H. Noh, S. H. Im, J. H. Heo, T. N. Mandal and S. I. Seok, *Nano Lett.*, 2013, **13**, 1764–1769.

225 S. Colella, E. Mosconi, P. Fedeli, A. Listorti, F. Orlandi, P. Ferro, T. Besagni, A. Rizzo, G. Calestani, G. Gigli, F. D. Angelis, R. Mosca and F. Gazza, *Chem. Mater.*, 2013, **25**, 4613.

226 F. Deschler, M. Price, S. Pathak, L. E. Klintberg, D. D. Jarausch, R. Higler, S. Hüttner, T. Leijtens, S. D. Stranks, H. J. Snaith, M. Atatüre, R. T. Phillips and R. H. Friend, *J. Phys. Chem. Lett.*, 2014, **5**, 1421–1426.

227 A. Kojima, K. Teshima, Y. Shirai and T. Miyasaka, *J. Am. Chem. Soc.*, 2009, **131**, 6050–6051.

228 C. Andrei, E. Lestini, S. Crosbie, C. D. Frein, T. O. Reilly and D. Zerulla, *PLoS One*, 2014, **9**, 1–12.

229 N. Chander, P. Singh, A. F. Khan, V. Dutta and V. K. Komarala, *Thin Solid Films*, 2014, **568**, 74–80.

230 B. Ding, M. Yang, B. J. Lee and J.-K. Lee, *RSC Adv.*, 2013, **3**, 9690–9697.

231 S. P. Lim, A. Pandikumar, N. M. Huang and H. N. Lim, *RSC Adv.*, 2014, **4**, 38111–38118.

232 J. T. Park, W. S. Chi, H. Jeon and J. H. Kim, *Nanoscale*, 2014, **6**, 2718–2729.

233 P. Ramasamy and J. Kim, *Chem. Commun.*, 2014, **50**, 879–881.

234 Y. Wang, J. Zhai and Y. Song, *RSC Adv.*, 2014, **5**, 210–214.

235 Q. Xu, F. Liu, W. Meng and Y. Huang, *Opt. Express*, 2012, **20**, 898–907.

This journal is © The Royal Society of Chemistry 2016

Energy Environ. Sci., 2016, **9**, 1577–1601 | 1601